HOKKAIDO UNIVERSITY

A study on uncoupled heterogenous multimode multicore fiber of two-ring core layout with 125 μm cladding diameter

（125 μm クラッド径を有する 2 リングコア配置非結合型異種マルチモードマルチコアファイバ に関する研究）

Zheyu Zhao

Information and Communication Photonics Laboratory

Graduate School of Information Science and Technology

Hokkaido University

Contents

Copyright Notice

This thesis summarizes and analyzes, and reorganizes based on the following papers.

- Z. Zhao, Y. Wang, T. Sato, T. Fujisawa, and K. Saitoh, “Investigation of heterogeneous step-index 2LP-mode multi-core fibers based on a two-ring layout with standard cladding diameter,” Opt. Continuum 2, 1137-1147 (2023), https://doi.org/10.1364/OPTCON.482118 .
- Z. Zhao, T. Sato, T. Fujisawa, T. Iwaya, Y. Sagae, T. Sakamoto, T. Matsui, K. Nakajima, and K. Saitoh, “Investigation of double-cladding heterogeneous step-index 2LP-mode multicore fiber with a two-ring layout,” J. Opt. Soc. Am. B 40, 2511-2518 (2023), https://doi.org/10.1364/JOSAB.498185 .

Chapter 1. Introduction

Optical communication technology has increased the transmission capacity of optical fibers by three orders of magnitude in recent years, enabling transmission of several Tbit per second. As data traffic grows at a rate between 40% and 70% each year, the future backbone must be able to handle more than Pbit/s per fiber. However, the traditional single-mode single-core fiber (SM-SCF) can deliver a maximum data transmission capacity of 100 Tbit/s [1], which is somewhat insufficient to cope with data growth, so new technologies are needed to increase data transmission capacity.

A growing amount of attention is being paid to Space Division Multiplexing (SDM), Wavelength Division Multiplexing (WDM), and Time Division Multiplexing (TDM) technology for optical communication. Compared to WDM, which utilizes different wavelengths, and TDM, which utilizes different time slots, SDM utilizes spatial dimensions to increase data transmission capacity [2]. As spatial diversity increases communication throughput, SDM makes high-capacity optical communication systems much more efficient, making it the ideal solution for expanding capacity. SDM is a proposed solution to boost capacity in optical communication, moving beyond conventional SM-SCF[1]. Multi-core fibers (MCFs), which consist of several cores enclosed within a single fiber cladding, have undergone extensive research and are considered a viable option for SDM transmission.

Multimode multicore fibers (MM-MCFs) are a type of optical fiber technology that combines the use of multiple cores within a single fiber with the capability to support multimode in each core. This design allows for increased data transmission capacity and efficiency compared to traditional SM-SCF [3]. This technology is seen as a potential solution for scaling up the spatial channel count (SCC) by integrating multiple modes with multiple cores. Research has delved into MCFs with increased cladding diameters to accommodate more cores. Notably, some MM-MCFs with SCC surpassing 100 have been reported [4][5][6], featuring cladding diameters larger than 300 μm. However, due to its superior mechanical reliability, the industry standard 125-μm cladding diameter is often preferred, especially in situations requiring tight bends [7]. Moreover, MCFs with this standard diameter

are compatible with existing optical cables, connector interfaces, and conventional optical components [8]. They also benefit from established splicing and cabling technologies [9], which significantly reduce overall manufacturing costs.

One significant challenge in MCFs is inter-core crosstalk (XT), which causes signal distortion and imposes limitations on transmission distance, capacity, and modulation formats [10]. XT between the highest order modes needs to be concerned because the XT between the highest order modes is larger than the XT among other combination of modes [11]. Various approaches have been introduced to mitigate XT, including cores with low refractive index structures [9][12][13]. These structures aim to enhance mode confinement or reduce mode field overlap. Still, they often involve complex and expensive fabrication processes due to their micrometer-sized features and the need for a significant amount of fluorine dopant [14].

Alternatively, heterogeneous MCFs (Hetero-MCFs), which consist of non-identical cores [7], have been proposed to achieve lower XT. Slight variations in core radii and refractive indices in Hetero-MCFs can significantly reduce XT. Compared to homogeneous MCFs (Homo-MCFs), where all cores are identical [9], non-identical cores in Hetero-MCFs can be more densely packed within a limited cladding diameter. Simple heterogeneous step-index (SI) cores offer a potential solution to reduce fabrication complexity and costs while maintaining sufficiently low XT. Therefore, this study highlights the utilization of non-identical SI cores in the design of 2LP-mode-MCFs within the standard 125-μm cladding diameter. This strategy is expected to increase the SCC, potentially reducing fabrication complexities and costs while achieving a higher SCC than previously reported 125-μm cladding MCFs [15-23].

This thesis is organized as follows:

In Chapter 2, the primary focus is on elucidating the analytical expression for the mode coupling coefficient between non-identical Step-Index (SI) cores, a pivotal element in the context of this paper. The methodology for estimating inter-core XT between such non-identical cores is outlined, showcasing its practical application in estimating XT within heterogeneous step-index multicore fibers (Hetero-SI-MCF). The introduced expressions are then applied to illustrate the calculation of XT between modes essential for this study, utilizing the case of a conventional Hetero-

SI-MCF designed with a standard 125 μm cladding diameter.

Moving on to Chapter 3, a novel approach is proposed through a two-ring core layout to enhance conventional Hetero-SI-MCFs. By strategically reducing the outer cladding thickness (T_C) of cores with a higher core refractive index, the core pitch (Λ) is expanded, resulting in lower XT values. The improvements in the two-ring core layout are thoroughly discussed and compared to those observed in their conventional counterparts. With the two-ring core allocation, it is demonstrated that the standard cladding diameter can effectively support 8 and 6 cores with sufficiently low XT for long-haul transmission in the C-band, respectively.

Chapter 4 introduces an innovative concept double-cladding to address the challenge of loss in outer cores of Hetero-SI-MCFs employing a two-ring core layout. In this design, the outer layer of cladding, featuring a higher refractive index than the standard fiber cladding, occupies the outermost part of the structure. This strategic addition allows for further expansion of the core pitch (Λ), leading to lower XT values. The proposed double-cladding approach convincingly demonstrates that the standard cladding diameter can support up to 10 cores with low XT for C-band transmission.

Chapter 5 highlights potential avenues for subsequent research within the scope of this study, particularly concentrating on the 4LP-mode and the C+L-band phases. The discourse extends to assessing the viability and practicality of undertaking further investigations and explorations centered around these specific wavelength bands and mode configurations. The outcomes of the brief analysis in this chapter underscore the favorable applicability of the two-ring core layout within the C+L-band and in the context of the 4LP-mode.

Chapter 6 serves as a comprehensive summary, encapsulating the key findings and contributions presented throughout the thesis.

Chapter 2. Estimation of XT analysis

The importance of calculating XT in the evaluation of fiber optic performance cannot be overstated. XT, denoting the interference that occurs between multiple signal paths within a fiber optic cable, plays a pivotal role in influencing the quality and efficiency of signal transmission. The accurate calculation of XT is crucial for a comprehensive assessment of the fiber's overall performance, encompassing critical aspects such as data transmission capacity, signal integrity, and reliability. This study is specifically designed to meticulously investigate and quantify the effectiveness of the proposed fiber structure by employing precise calculations to determine the extent of fiber XT. Through these calculations, we aim to gain deeper insights into the performance characteristics of the fiber and evaluate its potential impact on signal quality and overall transmission efficiency.

We begin this comprehensive chapter by presenting elaborate analytical expressions, which were meticulously derived for the mode coupling coefficients between identical Step-Index (SI) cores. Our subsequent investigations are based on the framework established in this foundational step. Based on these expressions, we investigate the estimation of inter-core XT values within heterogeneous step-index multi-core fibers (Hetero-SI-MCF). The application of these expressions to estimate XT serves as a crucial precursor to the in-depth analysis conducted in this study.

A Finite Element Method (FEM) is used to analyze guided modes within the fiber structure using the commercial software program COMSOL. Through the use of this sophisticated simulation tool, a comprehensive exploration of guided modes is possible, providing a detailed and accurate representation of the optical behavior within the Hetero-SI-MCF. The chapter contributes to our research's methodological transparency and rigor by providing an overview of the analytical and computational processes used to investigate Hetero-SI-MCFs.

2.1. *Definition of XT for two non-identical cores*

It is known that, as illustrated by Fig. 1, the XT of Hetero-MCF considerably decreases when the bending radius (R_b) becomes larger than a critical value (R_{pk}), and the XT converges on a certain value for enough larger R_b [9][24].

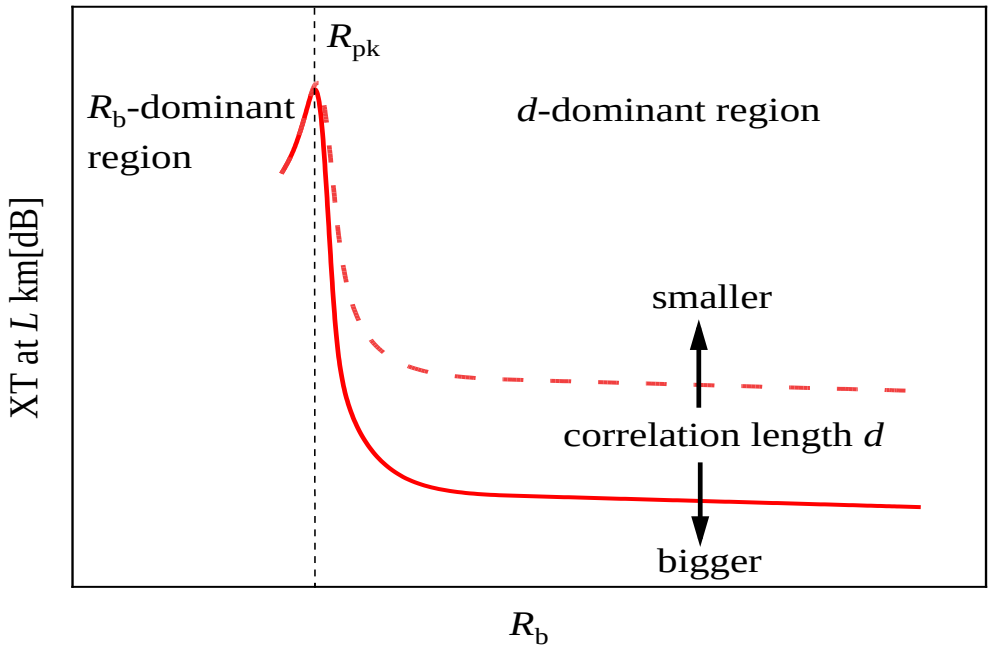

Fig. 1. Schematic of XT behavior as a function of R_b with correlation lengths d as parameters.

Different equations have to be used depending on R_b and R_{pk} to reflect this effect in the calculation of XT. The critical bending radius for the XT between p-th and q-th modes can be expressed as [21]

$$R_{pk} = \frac{\beta}{|\Delta\beta_{pq}|}\Lambda, \tag{1}$$

where Λ is core pitch, β is the mean of propagation constants of p-th and q-th modes, $\Delta\beta_{pq}$ is the difference of β between p-th and q-th propagation modes. If $R_b > R_{pk}$ and the XT is very small, no phase-matching point arises [25][26]. XT in MCFs can be evaluated by the coupled mode theory with random phase function [27]. The random process can be characterized by an autocorrelation function and correlation length d. The autocorrelation function is usually modeled by the exponential

autocorrelation function, and the averaged power-coupling coefficient can be given by [26]

$$\bar{h}_{pq} = \sqrt{2}K_{pq}^2 d\left[\frac{1}{\sqrt{a(b+\sqrt{ac})}} + \frac{1}{\sqrt{c(b+\sqrt{ac})}}\right] \tag{2}$$

with

$$a = 1 + (\Delta\beta_{pq} d - \frac{B_{pq} d}{R_b})^2 \tag{3}$$

$$b = 1 + (\Delta\beta_{pq} d)^2 - (\frac{B_{pq} d}{R_b})^2 \tag{4}$$

$$c = 1 + (\Delta\beta_{pq} d + \frac{B_{pq} d}{R_b})^2 \tag{5}$$

$$B_{pq} = \sqrt{(\beta_p x_p - \beta_q x_q)^2 + (\beta_p y_p - \beta_q y_q)^2}, \tag{6}$$

where x_p and y_p are the x and y coordinates of the center of core which propagates the p-th mode, respectively. K_{pq} is the mean value of mode coupling coefficients for p-th and q-th modes, namely $(\kappa_{pq} + \kappa_{qp})/2$ [28], and the mode-coupling coefficient with the overlap integral of electromagnetic fields is generally written as follows [29]:

$$\kappa_{pq} = \frac{\omega\varepsilon_0 \int_{-\infty}^{\infty}\int_{-\infty}^{\infty} (N^2 - N_q^2)\boldsymbol{E}_p^* \boldsymbol{E}_q dxdy}{\int_{-\infty}^{\infty}\int_{-\infty}^{\infty} \boldsymbol{u}_z(\boldsymbol{E}_p^* \times \boldsymbol{H}_p + \boldsymbol{E}_q \times \boldsymbol{H}_q^*)dxdy} \tag{7}$$

where κ_{pq} represents the mode-coupling coefficient from the core, which propagates the q-th mode, to the core which propagates the p-th mode. ω is the angular frequency of the electromagnetic fields, and ε_0 is the permittivity of the vacuum. $\boldsymbol{E}$ and $\boldsymbol{H}$ stand for the electric and magnetic fields, respectively, * denotes the complex conjugate, and $\boldsymbol{u}_z$ represents the unit vector of the z-axis. N^2 denotes the refractive index distribution in the entire coupled region, and N_q^2 represents the refractive index distribution of the core, which propagates the q-th mode, which consists of the core and the cladding region. The averaged XT can be given by

$$XT_{pq}\,[\mathrm{dB}] = 10\log_{10}\left(\tanh(\bar{h}_{pq}L)\right) \tag{8}$$

L is the transmission length. As shown in Fig. 1 illustrating the XT behavior, the correlation length d will be a dominating parameter compared with R_b for $R_\mathrm{b} > R_\mathrm{pk}$. In fact, d cannot be determined because this value depends on such as fabrication precision. The settings of d that make the calculated results match the experimental results are different. The results of [3], [30] show that the estimated correlation length exceeds 1 m. Note that although we fixed a correlation length of d = 1 m consistent with that used in the previous single-mode fiber study [15], which used the same core layout as our research, d actually depends on the actual manufacturing process. Especially in the d-dominant region, the increase (or decrease) of d reflects the decrease (or increase) of XT, because the XT is approximated by XT $\propto 1/d$. On the contrary, when the phase-matching condition is satisfied (i.e., when $R_\mathrm{b} < R_\mathrm{pk}$), the XT strongly depends on R_b, as shown in Fig. 1. To suppress the XT, the use of a d-dominant region ($R_\mathrm{b} > R_\mathrm{pk}$) is preferable rather than an R_b-dominant region ($R_\mathrm{b} < R_\mathrm{pk}$). By increasing Λ, R_pk will shift to the larger R_b although the XT defined by Eq. (8) will be small due to lowering K_{pq}, which is a tradeoff relationship. Furthermore, MCFs that have a limited cladding diameter (CD) must also consider a tradeoff between Λ and outer cladding thickness, which will be discussed next. Noting that, since the XT linearly increases as seen in Eq. (8), we express the XT_{pq} [dB] for 1 km as XT_{pq} [dB/km] in this paper, that is, XT_{pq} [dB/km] = XT_{pq} [dB]$|_{L\,=\,1\ \mathrm{km}}$.

2.2. *XT of Hetero-SI-FM-MCFs with one-ring layout for C-band*

Compared to the previously mentioned Eq. (1), the R_pk is also given by the following equation.

$$R_\mathrm{pk} = \frac{n_\mathrm{eff}}{\left|\Delta n_{\mathrm{eff},\,pq}\right|}\Lambda, \tag{9}$$

where n_eff is the effective index of the mode, Δn_eff is the effective index difference between the core, which propagates the q-th mode, and the core, which propagates

the p-th mode, and Λ is the core pitch. Heterogeneous core design means that the n_{eff} is different for adjacent cores. The main target is to find cores with a large enough Δn_{eff}. Ensuring 2LP-mode functionality necessitates cores that satisfy specific loss criteria, a major concern is the excessive loss (*EL*) in cores, mainly stemming from macro-bending loss (*BL*) due to the fiber coating's high refractive index [31]. The coating material's refractive index (n_{coat}) varies between 1.465 and 1.485, influencing core loss [32]. However, controlling n_{coat} in actual fibers is challenging, leading to a standard simulation value of 1.486 [31]. In our study, we also adopt this fixed value of 1.486 for n_{coat} when evaluating core loss. Additionally, our research consistently uses a cladding refractive index of 1.45, aligning with that of pure silica.

Decision of core parameters

Figure 2 illustrates the typical approach for selecting cores. Cores varying in core radius (a) and relative refractive indices (Δ), exhibit different effective areas (A_{eff}). To ensure 2LP-mode functionality in C-band, the cutoff limits of the LP_{21} mode for various T_{C} values are depicted by colored dashed lines. These are calculated based on the *BL* of the LP_{21} mode being greater than 1 dB/m at a wavelength of 1530 nm and a bend radius (R_{b}) of 140 mm. Meanwhile, the colored solid lines indicate the *EL* thresholds of the LP_{11} mode for different T_{C}s, determined under the condition that the *BL* of LP_{11} mode remains below 0.01 dB/km at 1565 nm with the same R_{b} [8].

When the T_{C} of the core is 35 μm, the region below the green dashed line represents the parameters in the core that meet the cutoff limit for the LP_{21} mode, while the region above the green solid line represents the parameters in the core that meet the LP_{11} mode *EL* limit. In Figure 2, all the shaded region's core parameters are found to meet all the requirements of the design for a fiber with a 2LP-mode. To achieve uniform transmission characteristics and minimize splice losses [7], it's essential to choose cores with comparable A_{eff} values. For applications in the C-band, we opt for cores with an A_{eff} of 80 μm^2 at a wavelength of 1550 nm. This specification aligns with the standard recommendation for single-core single-mode

fibers and is indicated by the black dot-dashed line in Figure 2.

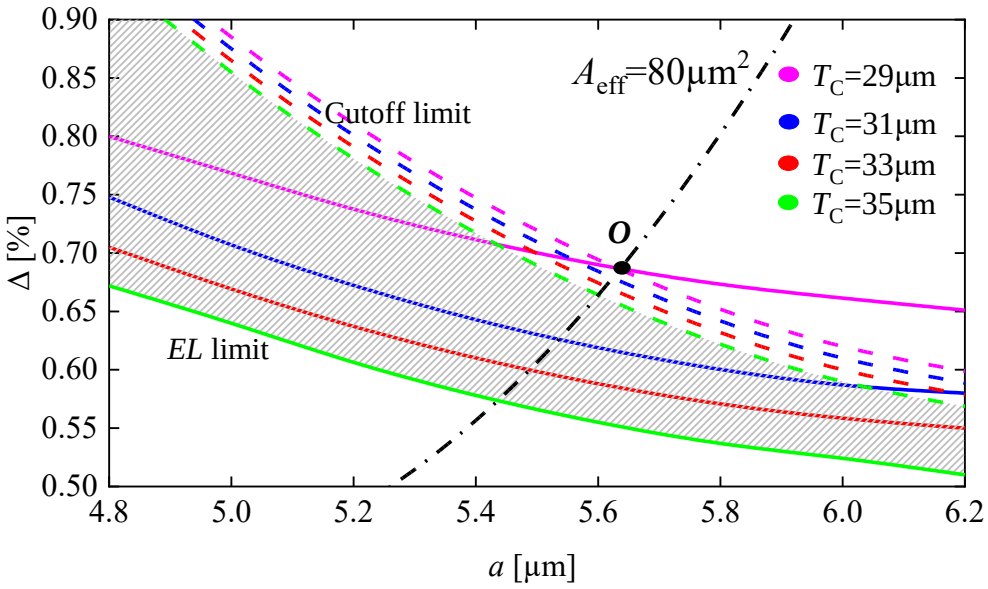

Fig. 2. Relationship between the core parameters and effective indices for the C-band: T_C = 29, 31, 33, and 35 μm.

The *BL* of cores is significantly influenced by the thickness of the outer cladding (T_C) [31]. Therefore, our approach begins with a T_C of 35 μm, incrementally decreasing by 1 μm to determine suitable core selections for the fiber design. In Fig. 2, for a T_C of 29 μm, the intersection point of the *EL* limit, cutoff limit, and the line representing A_{eff} = 80 μm^2 is marked by the black dot (point *O*). This suggests that this particular core is suitable for creating homogeneous step-index MCFs (Homo-SI-MCFs) with a T_C of 29 μm. From these curves, it's apparent that only the cores lying within the area bounded by the dashed and solid lines of the same color and along the A_{eff}= 80 μm^2 line are suitable for fiber design. This specific area is referred to as the effective core region (*ECR*), exemplified by the region between points *M* and *N* in Fig. 3 (a).

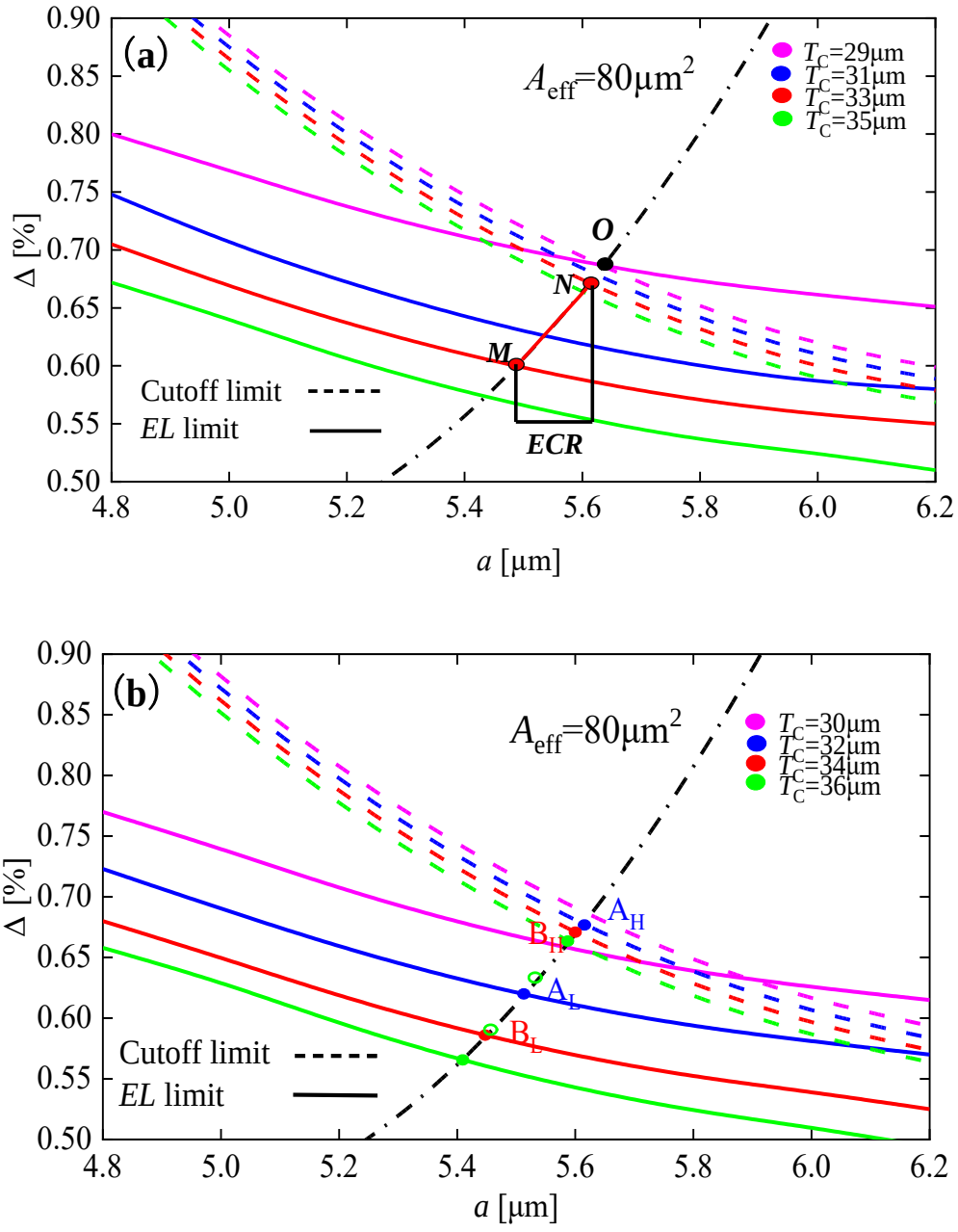

Fig. 3. Relationship between the core parameters and effective indices for the C-band: (a) T_C = 29, 31, 33, and 35 μm; (b) T_C = 30, 32, 34, and 36 μm.

Simulation of XT

In Fig. 3 (a), It's observed that with increasing T_C, both the *EL* and cutoff limits shift towards the region with lower core refractive indices, with the *EL* limit moving more swiftly than the cutoff limit. This is attributed to the LP_{11} mode's loss being

more sensitive to T_C changes compared to the LP_{21} mode, resulting in an expanded *ECR*. This expansion aids in selecting diverse cores for designing Hetero-SI-MCFs. Considering potential fabrication inaccuracies in core radius a and core Δ, we include cores that deviate slightly from these limits to illustrate the XT error. One such core has a radius 0.05 μm smaller and a core Δ 0.025% lower than the upper limit core, and another has a radius 0.05 μm larger and a core Δ 0.025% higher than the lower limit core. These cores, still approximating an A_{eff} of 80 μm^2, are shown as green hollow circles in Fig. 3 (b), matching the colors of the cores at the limits for the same T_C value.

According to Eq. (9), a higher Δn_{eff} value leads to a smaller R_{pk}, implying a more rapid decrease in XT. Consequently, we design Hetero-SI-MCFs using one core at the upper limit and another at the lower limit of the *ECR*. For instance, in Fig. 3 (b), the *ECR* edge core parameters for a T_C of 32 μm are represented by two blue dots (cores A_H and A_L), and for $T_C = 34$ μm by two red dots (cores B_H and BL). Here, 'H' and 'L' denote the upper and lower *ECR* limits, respectively. Due to stringent loss constraints, these cores are arranged in a one-ring layout within the fiber cladding, as depicted in Fig. 4, where the total number of cores (N) is 6.

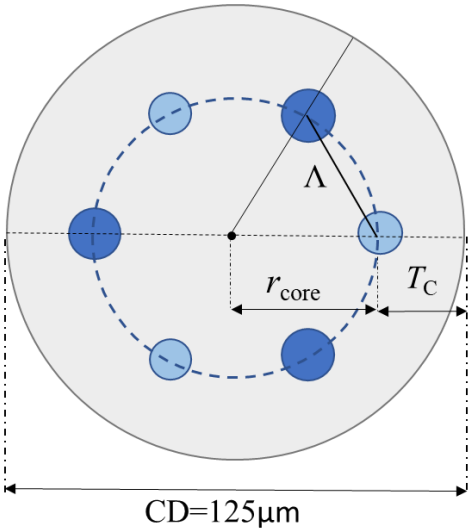

Fig. 4. Cross sections of the designed Hetero-SI-MCFs with non-identical cores.

Since the center of this circle coincides with that of the 125-μm cladding, the distance between the center of the core and the outer layer of cladding T_C for all cores is the same as

$$T_C = 62.5 - r_{core}, \tag{10}$$

where r_{core} is the distance between the center of the fiber and that of each core. When the number of cores is N (N is an even number and $N \geq 2$), and the center of 125-μm diameter cladding is set as the origin of the polar coordinate system, the coordinate of the i-th ($i = 1, \ldots, N$) core position is expressed as (r_{core}, θ_i), where $\theta_i = (2\pi/N)i$ and the r_{core} is given as

$$r_{core} = \frac{\Lambda}{2\sin\left(\frac{\pi}{N}\right)}. \tag{11}$$

To examine these two core parameter sets, we plot XTs for adjacent cores as a function of R_b in Figs. 5 (a) and (b) by calculating Eq. (8), where $N = 6$, $\lambda = 1550$ nm, and $d = 1$ m. $XT_{11\text{-}11}$ and $XT_{01\text{-}01}$ denote the XT between the LP_{11} and LP_{01} modes in two cores, respectively. $XT_{11\text{-}01}$ ($XT_{01\text{-}11}$) denotes the XT between the LP_{11} (LP_{01}) mode in the lower limit core and the LP_{01} (LP_{11}) mode in the higher limit core. We can see that, as expected, $XT_{11\text{-}11}$ is the largest XT among all combinations of modes. When $R_b > 100$ mm, the XT for $T_C = 32$ μm is better than that for $T_C = 34$ μm. However, a relatively large R_{pk} can be seen for $T_C = 32$ μm, this is because the Δn_{eff} between cores A_H and A_L is smaller than that between cores B_H and B_L.

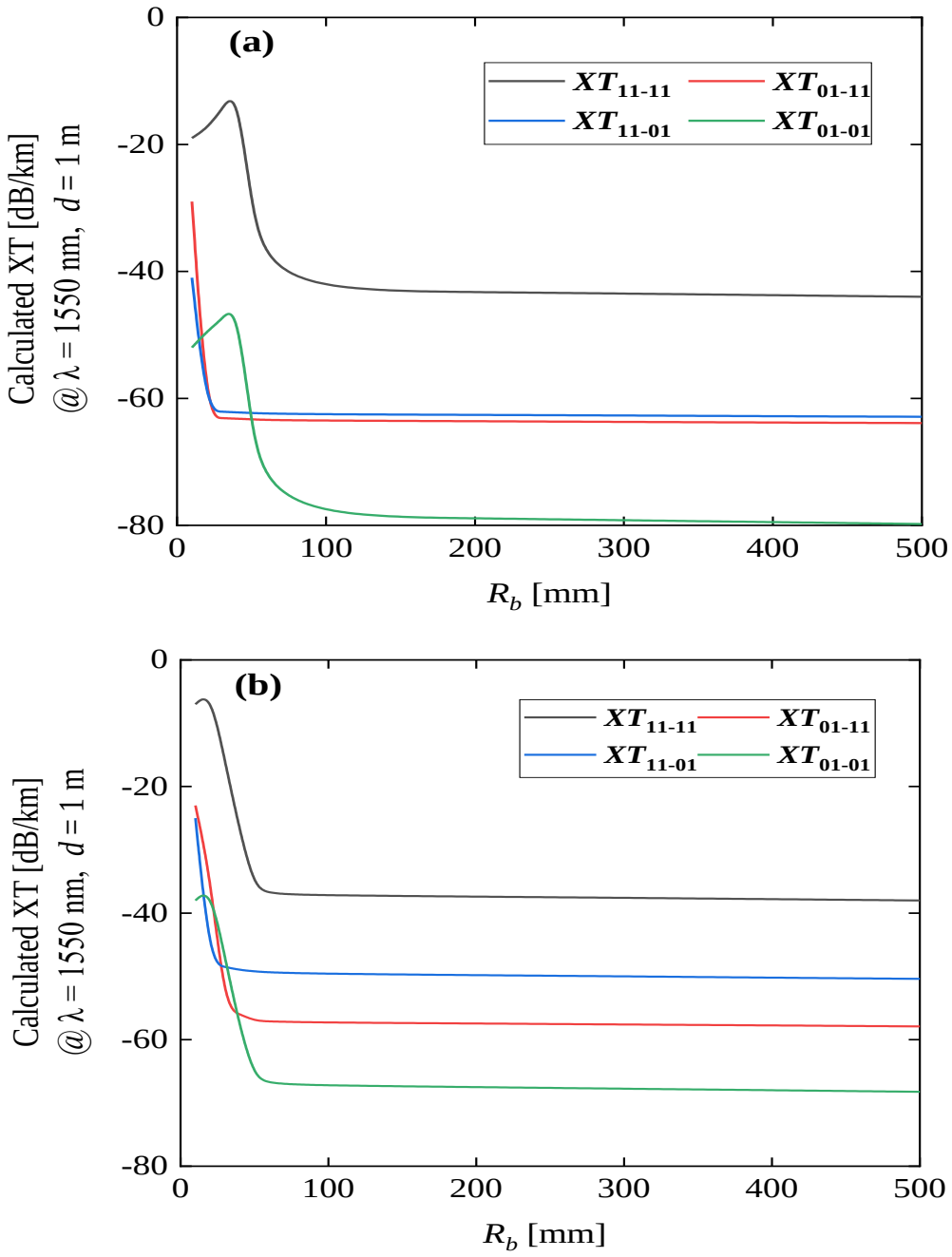

Fig. 5. XTs as a function of R_b, where N = 6: (a) between cores A_H and A_L (T_C = 32 μm); (b) between cores B_H and B_L (T_C = 34 μm).

The dependency of $XT_{11\text{-}11}$ at R_b = 140 mm on T_C is shown in Fig. 6, where N = 6, λ = 1550 nm, and d = 1 m, and error bars indicate the XT errors due to the core parameter variations mentioned before. We can see that $XT_{11\text{-}11}$ is suppressed well when $T_C \geq 31$ μm because $R_{pk} < 140$ mm satisfies. The minimum $XT_{11\text{-}11}$ is −42.7 dB/km when T_C = 31 μm. As T_C further increases, the core pitch Λ decreases, and

then the mode coupling strength K_{pq} in Eq. (2) increases, resulting in the degradation of XT. Such a tendency is similar to single-mode Hetero-MCFs [15].

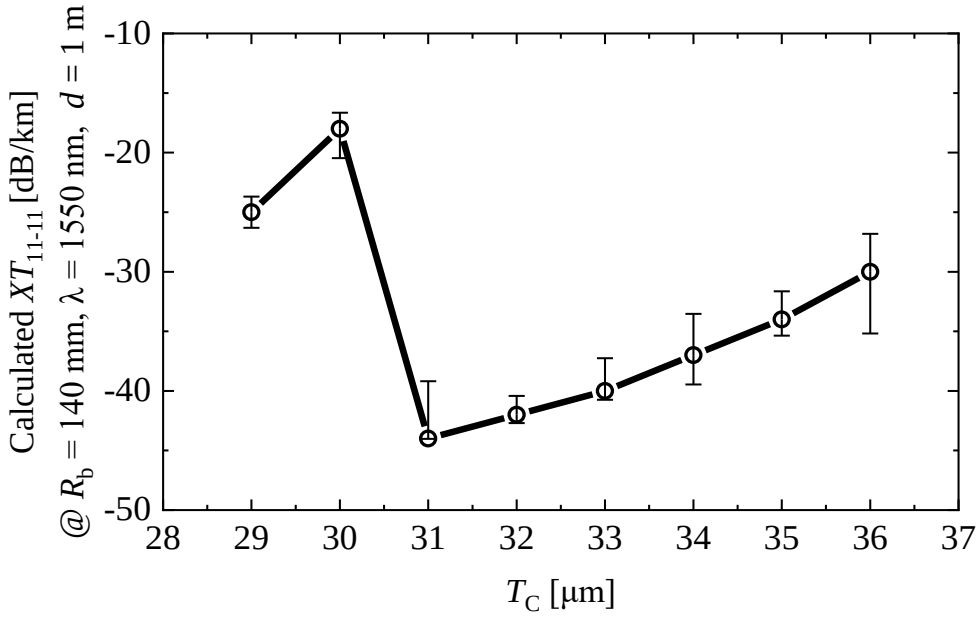

Fig. 6. The XT as a function of T_C, where N = 6, λ = 1550 nm, d = 1 m, and R_b = 140 mm.

If we consider the quadrature phase shift keying (QPSK), 16 quadrature amplitude modulation (QAM), and 64QAM format signals, the allowable XT (XT_{al}) is less than −16, − 24, and −32 dB, respectively [10], and hence, the maximum transmission length L_{max} is estimated by

$$L_{max}\,[\mathrm{km}] = 10^{\frac{XT_{al}\,[\mathrm{dB}] - XT_{11\text{-}11}\,[\mathrm{dB/km}]}{10}}. \tag{12}$$

Fig. 7 shows L_{QPSK}, L_{16QAM}, and L_{64QAM} corresponding to Fig. 6. When T_C = 31 μm, L_{QPSK}, L_{16QAM}, and L_{64QAM} are 680, 108, and 17 km, respectively. Note that XTs are calculated at λ = 1550 nm, and therefore, it is expected that the maximum distances would be practically much lower for longer wavelengths in C-band.

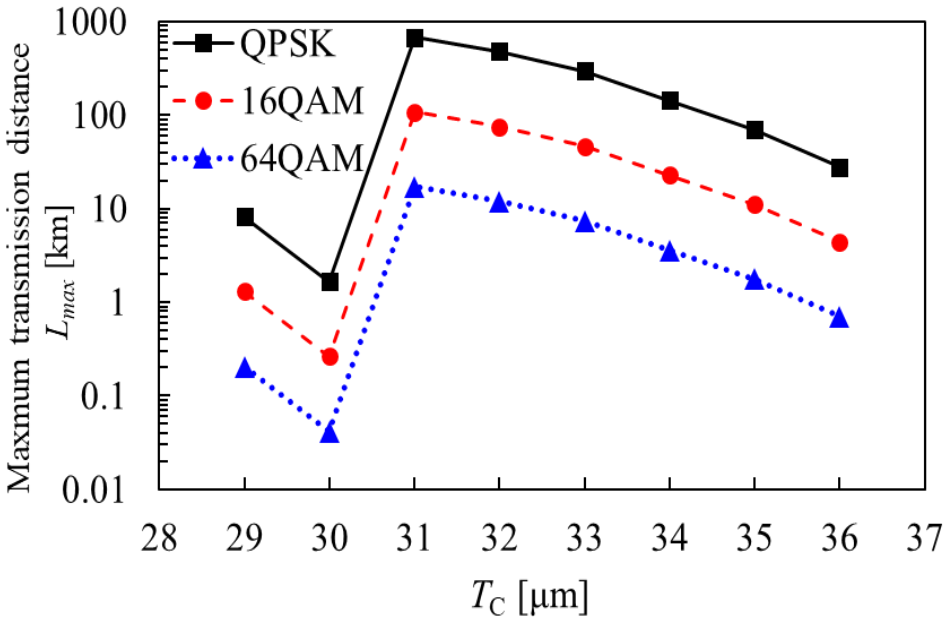

Fig. 7. The Maximum transmission distance L_{QPSK}, L_{16QAM}, and L_{64QAM} as a function of T_C, where N = 6, λ = 1550 nm, d = 1 m, and R_b = 140 mm.

Therefore, for the C-band, by using the non-identical SI cores, the number of spatial channel count (SCC) is increased by 12, and the XT value exceeds that of the Hetero-SM-MCFs reported in Ref. [15].

2.3. *Conclusion*

An analytical expression for the XT between non-identical SI cores is clarified. Using the analytical expressions, the simple SI profile allows for the efficient arrangement of 6 distinct cores within a 125-μm cladding diameter, with each core capable of supporting three modes. This layout, utilizing a one-ring core design, is specifically tailored for use in the C-band. The main parameters of the designed one-ring 2LP-mode Hetero-SI-MCFs are listed in Table I.

Table. I Fiber parameters of the designed one-ring core layout Hetero-SI-MCFS

N	T_C [μm]	a [μm]	Δ [%]	Λ [μm]	$XT_{11\text{-}11}$ [dB/km]
6	31	5.62	0.679	31.5	−42.7
		5.54	0.627		

Chapter 3. Characteristics of 2LP-mode Hetero-SI-MCFs with two-ring core layout

3.1 Diagram of the two-ring core layout

Compared with Fig. 4 which shows the cross-section of the conventional Hetero-MCFs with one-ring core layout, where all the cores are equally allocated to a common circle whose center is the cladding center, which indicates all the cores have a common T_C, whereas Fig. 8 (a) and (b) shows the cross-section of the 6- and 8- core Hetero-MCFs with two-ring core layout which we used in this chapter, in which the cores with lower core refractive index (core L) and the cores with higher core refractive index (core H) are allocated to different circles respectively. Although core H moves outward slightly, its effect on *BL* is low due to its higher refractive index. It is important to note here that the T_C of cores H ($T_{C\text{-}H}$) could be smaller than that of cores L ($T_{C\text{-}L}$), and core H is relocated into an outward position, resulting in the enlargement of core pitch (Λ) for achieving lower XT. The Hetero-MCF based on the two-ring structure has the advantage of having a lower XT compared to the Hetero-MCF based on the conventional structure. Here, Λ_2 indicates the second nearest core pitch between the adjacent core L with a lower core refractive index in the two-ring core layout Hetero-MCFs.

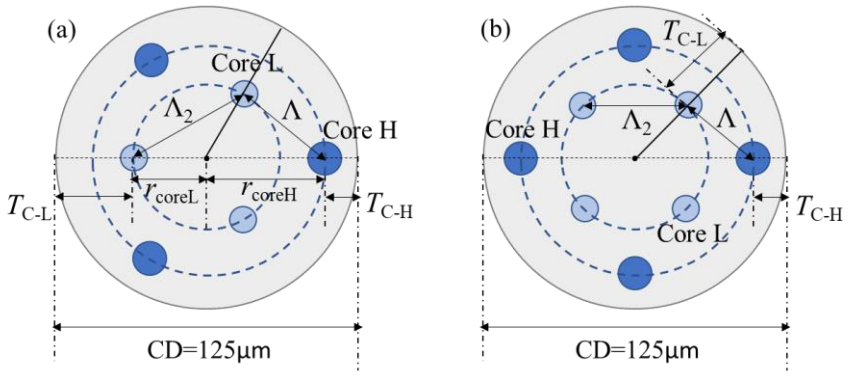

Fig. 8. Schematic of the Hetero-MCFs with two-ring core layout design. (a) 6-core Hetero-MCFs. (b) 8-core Hetero-MCFs.

For the core number N (N is an even number and $N \geq 4$), $T_{\text{C-H}}$ and $T_{\text{C-L}}$ can be expressed as

$$T_{\text{C-H, C-L}} = 62.5 - r_{\text{coreH, coreL}}, \tag{13}$$

where

$$r_{\text{coreH}} = \frac{\Lambda_2}{2\tan\left(\frac{2\pi}{N}\right)} + \sqrt{\Lambda^2 - \frac{\Lambda_2^2}{4}}, \tag{14}$$

$$r_{\text{coreL}} = \frac{\Lambda_2}{2\sin\left(\frac{2\pi}{N}\right)}. \tag{15}$$

The steps to design the Hetero-SI-MCFs are introduced in the following sections.

3.2 XT simulation of 2LP-mode Hetero-SI-MCFs with two-ring layout

Referring to Fig. 3 (a), here we use the green dotted core M and core N as examples to highlight the differences between the one-ring core layout and the two-ring layout Hetero-MCF design when T_C equals 35 μm.

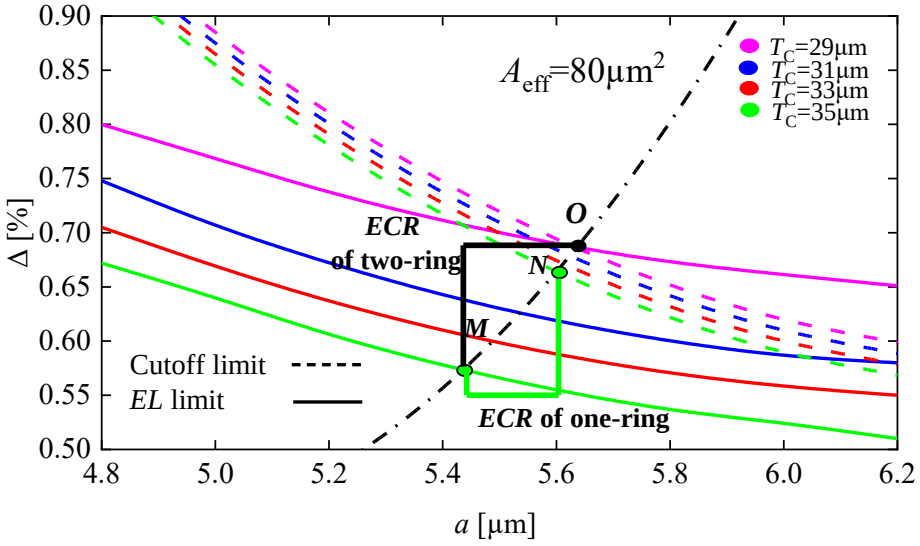

Fig. 9. Relationship between the core parameters and effective indices for the C-band, where T_C = 29, 31, 33, and 35 μm.

In the one-ring layout design, both core *M* and *N* are positioned on a common circle with T_C at 35 μm, meaning both $T_{C\text{-}L}$ and $T_{C\text{-}H}$ are equal to 35 μm, which is shown in Fig. 9 with green line parenthesis. However, in the two-ring layout design, while core *M* remains on the circle with $T_{C\text{-}L}$ at 35 μm, core *N* is relocated. This is because the reduction in $T_{C\text{-}H}$ allows for the placement of core *O*, marked by a black dot, on a circle with T_C at 29 μm, facilitated by the upward shift of the cutoff limit line, which is shown in Fig. 9 with black line parenthesis. Consequently, core H is fixed with $T_{C\text{-}H}$ at 29 μm in the two-ring core layout Hetero-SI-MCFs, with the core L determined by $T_{C\text{-}L}$ and positioned accordingly. It's important to note that changes in $T_{C\text{-}L}$ result in alterations of core L's parameters, as depicted by the various colored dots in Fig. 10, like points *A*, *B*, and *N*.

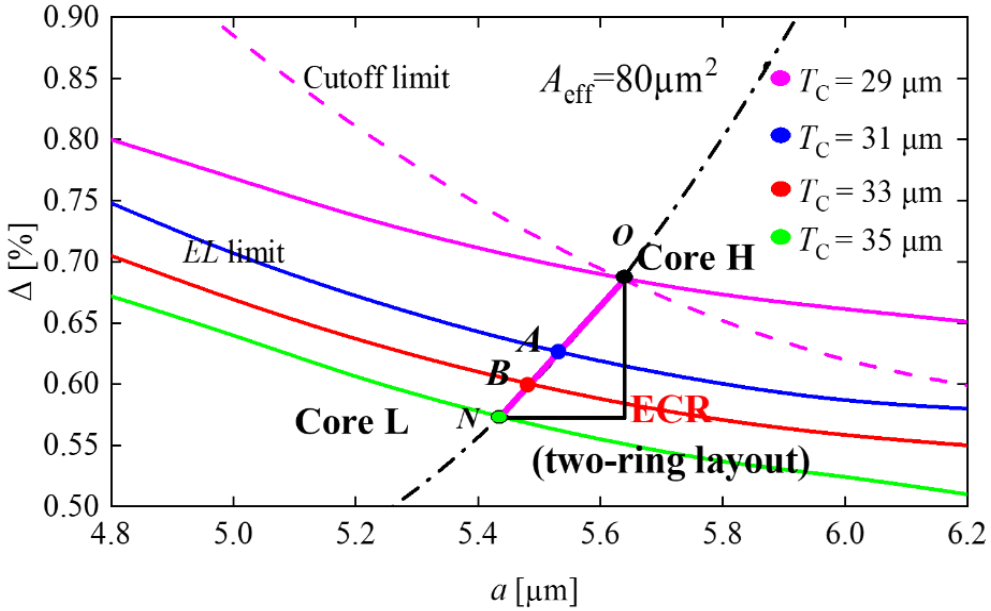

Fig. 10. Distribution of the core parameters for core H and core L for the C-band, where T_C = 29, 31, 33, and 35 μm.

Given that the XT in the one-ring structure 6-core fiber, discussed in Section 2.2, is low at −47 dB/km, our analysis begins with a 6-core fiber. Our goal is to analyze the improvements offered by the two-ring core layout and to investigate the feasibility of integrating up to 8 cores within the confines of the standard cladding diameter.

It's emphasized that in uncoupled MCFs with fabrication inconsistencies, random structural fluctuations are crucial in determining the XT. Therefore, it's

important to take these fabrication errors into account during the design phase of uncoupled MCFs [33]. In the context of the C-band, for cores positioned at the upper and lower limits of the *ECR*, an additional core is used for error analysis. The details of these additional cores are described in subsection 2. 2, which is denoted by circles colored identically to the cores at the respective limits, like the green hollow circles shown in Fig. 3 (b). The error bars derived from the parameters of these additional cores will be displayed in the next subsections.

6-core 2LP-mode Hetero-SI-MCF

As mentioned before, we should fix $T_{C\text{-}H}$ = 29 μm and change the parameter of core L by increasing $T_{C\text{-}L}$ from 29 μm. The XT distribution results shown in Fig. 5 reveal that the XT value is highest between the LP_{11} modes ($XT_{11\text{-}11}$) for 2LP-mode Hetero-SI-MCFs. Figure 11 shows the comparison of $XT_{11\text{-}11}$ between the Hetero- MCFs with the one-ring and two-ring layout, where N = 6, R_b = 140 mm, λ = 1550 nm, d = 1 m, and $T_{C\text{-}H}$ = 29 μm. $XT_{or,\,tr}$ represents the XT value of one-ring and two-ring layout, respectively. And 'H-L' denotes the XT between adjacent cores of core H and core L, and 'L-L' denotes the XT between nearest cores L.

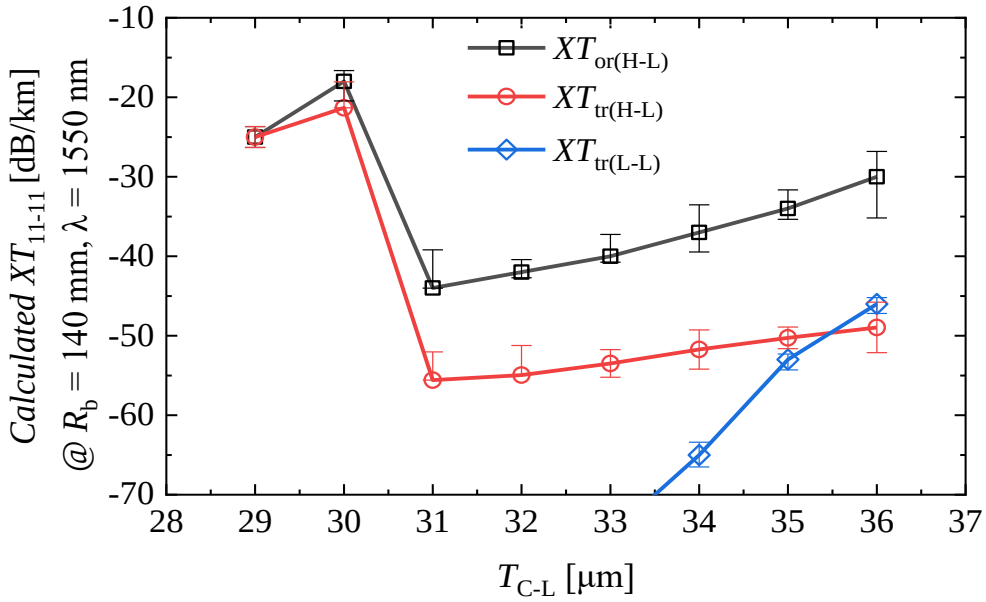

Fig. 11. Calculated $XT_{11\text{-}11}$ as functions of $T_{C\text{-}L}$ for C-band where N = 6, λ = 1550 nm, d = 1 m, and $T_{C\text{-}H}$ = 29 μm.

When T_C equals 29 μm, the XT for the Homo-SI-MCFs, designed with core *O*

indicated by the black dot in Fig. 3 (a), is graphed, leading to an equivalence XT value between XT_{or} and XT_{tr}. For T_C values greater than 29 μm, the $XT_{or(H-L)}$ for one-ring Hetero-SI-MCFs, which are designed with core combinations marked by similarly colored dots in Fig. 3 (a) and (b), is charted. Concurrently, the $XT_{tr(H-L)}$ for the Hetero-SI-MCFs with two-ring core layout, utilizing core *O* from Fig. 3 (a) and the core at the lower limit of the *ECR* for varying T_{C-L} values, is also graphed.

In the case of a 6-core configuration ($N = 6$), when the outer cladding thickness of cores with lower refractive index (T_{C-L}) is set at 30 μm, the R_{pk} for Hetero-MCFs exceeds 140 mm. Consequently, both the $XT_{or(H-L)}$ and $XT_{tr(H-L)}$ are in the higher range within the *R*-dominant region, as depicted in Figure 1. This indicates the importance of maintaining a sufficiently large effective refractive index difference (Δn_{eff}) to ensure that R_{pk} remains below a certain threshold. Upon adjusting T_{C-L} to 31 μm, R_{pk} falls below 140 mm, resulting in a significant decrease in both $XT_{or(H-L)}$ and $XT_{tr(H-L)}$ to ultra-low values. This shift occurs in the *d*-dominant region of Figure 1, emphasizing the critical role of T_{C-L} in influencing the bending radius and, consequently, the XT characteristics in Hetero-MCFs.

In one-ring layout Hetero-SI-MCFs, $XT_{or(H-L)}$ progressively increases with T_{C-L}. For all T_{C-L}, XTs of the two-ring layout are improved compared with those of one-ring layout. Such a tendency is similar to single-mode Hetero-MCFs [15]. Thus, we recommend the two-ring layout 6-core fiber design with T_{C-L} = 31 μm, targeting the most favorable $XT_{tr(H-L)}$ value of −51.2 dB/km for adjacent cores, indicating an improvement of 8.5 dB/km compared with the one-ring layout. This design is expected to support QPSK format signal transmission with a 1 dB XT penalty over several thousand kilometers [10], which is shown in Fig. 12. The $XT_{tr(L-L)}$ escalates rapidly with increasing T_{C-L} and surpasses $XT_{tr(H-L)}$ at T_{C-L} = 36 μm. Notably, because $XT_{tr(L-L)}$ is less than −70 dB/km for $T_{C-L} < 34$ μm, this portion of the blue line is omitted from Fig. 12.

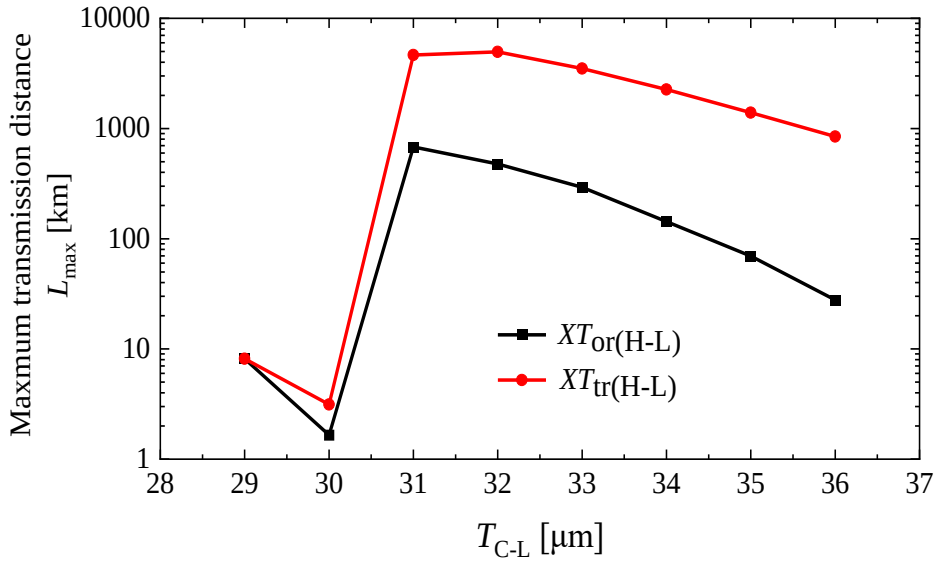

Fig. 12. Maximum transmission distance L_{QPSK} as a function of $T_{C\text{-}L}$.

8-core 2LP-mode Hetero-SI-MCF

For $N = 8$, the optimal $XT_{or(H\text{-}L)}$ value is observed at $T_{C\text{-}L} = 31$ μm, beyond which $XT_{or(H\text{-}L)}$ increases with increasing $T_{C\text{-}L}$. Conversely, for the two-ring core layout Hetero-SI-MCFs, the lowest $XT_{tr(H\text{-}L)}$ value is achieved at $T_{C\text{-}L} = 33$ μm, after which $XT_{tr(H\text{-}L)}$ too begins to rise with increasing $T_{C\text{-}L}$. Referring to Eq. (1) from Ref. [26], we note that in Hetero-SI-MCFs with one-ring core layout, the region with $T_{C\text{-}L} <$ 31 μm is dominated by $\Delta\beta_{pq}$, leading to a reduction in $XT_{or(H\text{-}L)}$. However, for $T_{C\text{-}L} >$ 31 μm, the influence of K_{pq} becomes predominant, causing an increase in $XT_{or(H\text{-}L)}$. Similarly, in the two-ring layout Hetero-SI-MCFs, the $T_{C\text{-}L} < 33$ μm region is influenced by $\Delta\beta_{pq}$, reducing $XT_{tr(H\text{-}L)}$, whereas the region with $T_{C\text{-}L} > 33$ μm is governed by K_{pq}, resulting in an increased $XT_{tr(H\text{-}L)}$.

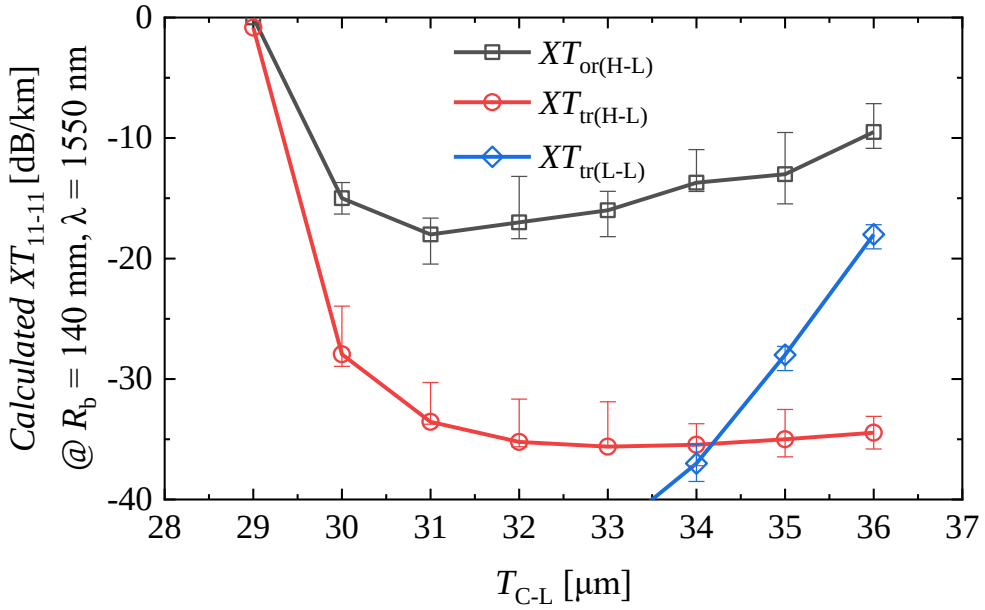

Fig. 13. Calculated $XT_{11\text{-}11}$ as functions of $T_{C\text{-}L}$ for C-band where $N = 8$, $\lambda =$ 1550 nm, $d = 1$ m, and $T_{C\text{-}H} = 29$ μm.

Drawing upon these research findings, we recommend the adoption of the 8-core fiber design with a two-ring core layout and a $T_{C\text{-}L}$ (outer cladding thickness of cores with lower refractive index) of 33 μm. This specific design is targeted to achieve the most favorable $XT_{tr(H\text{-}L)}$ value of −35.5 dB/km. It is anticipated that this configuration will be capable of supporting QPSK format signal transmission with a 1 dB XT penalty at distances around 100 km, as illustrated in Figure 14.

It's noteworthy that the $XT_{tr(L\text{-}L)}$ experiences a rapid escalation with increasing $T_{C\text{-}L}$, surpassing $XT_{tr(H\text{-}L)}$ at $T_{C\text{-}L} = 35$ μm. Since $XT_{tr(L\text{-}L)}$ is less than -40 dB/km for $T_{C\text{-}L} < 34$ μm, this portion of the blue line is omitted from Figure 14.

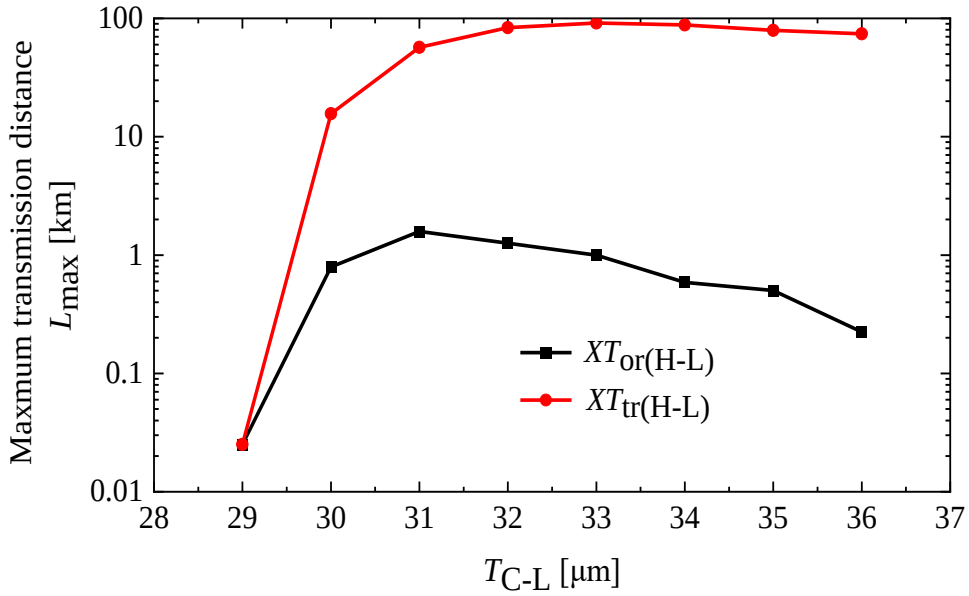

Fig. 14. Maximum transmission distance L_{QPSK} as a function of $T_{C\text{-}L}$.

The data from Figs. 11 and 13 consistently show that $XT_{tr(H\text{-}L)}$ is less than $XT_{or(H\text{-}L)}$ across all scenarios, highlighting the effectiveness of the two-ring core layout structure in enhancing the XT performance of Hetero-SI-MCFs.

3.3 Conclusion

In this study, a two-ring core layout has been implemented for core allocation in Hetero-MCFs. As a result, 6-core fibers are developed with low inter-core XT. Despite all of this, the cladding diameter (CD) remains within the standard 125 μm and an SI profile is employed.

Additionally, the investigation demonstrates that the standard CD has the ability to support not only six cores with such low XT, but can also support up to eight simple SI non-identical cores, all while maintaining XT levels suitable for C-band applications. The specific core parameters for these designed Hetero-SI-MCFs, featuring the two-ring layout optimized for C-band use, are meticulously detailed in Table II. This comprehensive table provides a clear delineation of core characteristics, with core *O* identified as possessing the highest core refractive index, visually marked by the black dot in Figure 10. In the case of the 6-core fiber, core

S_L is specifically designated as the one with a lower core refractive index, while for the 8-core fiber, core E_L assumes the role of the core with the lower refractive index. Table III further elucidates the primary parameters of these specifically modified Hetero-SI-MCFs, purposefully designed for optimal performance in C-band applications.

Table. II Core parameters for designed Hetero-SI-MCF

Core name	a [μm]	Δ [%]	A_{eff} [μm^2]
O	5.66	0.683	80.1
S_L	5.65	0.678	80.1
E_L	5.58	0.641	80.1

Table. III Fiber parameters of the designed Hetero-SI-MCFS

N	$T_{C\text{-}H}$ [μm]	$T_{C\text{-}L}$ [μm]	Λ [μm]	Λ_2 [μm]	$XT_{11\text{-}11}$ [dB/km]
6	29	31	32.5	54.6	−51.2
8	29	33	24.4	41.7	−35.5

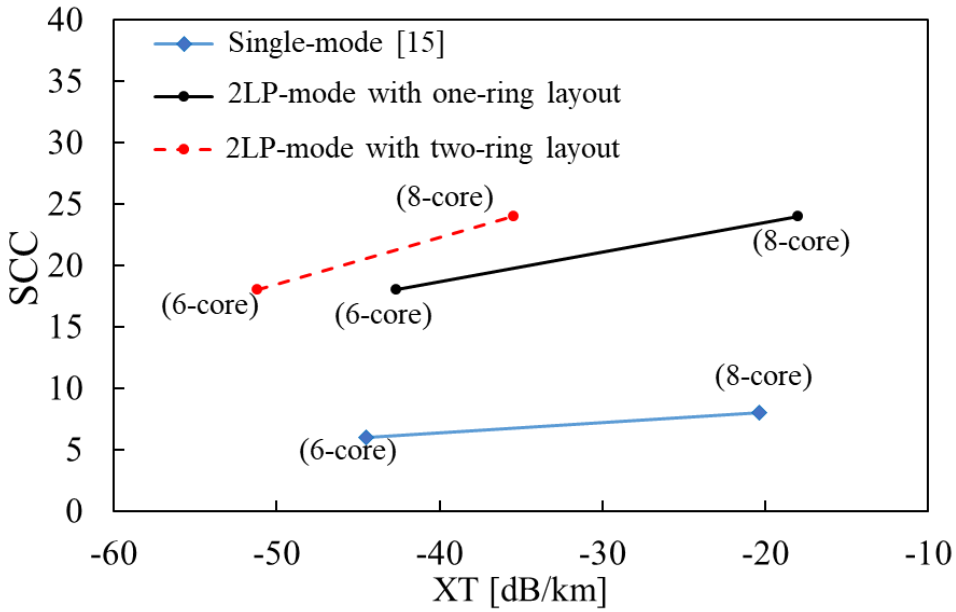

Fig. 15. Comparison of SCC and XT between single-mode and 2LP-mode Hetero MCFs.

Although there has been an increasing body of research on MCFs over the last few years, there has been a significant lack of research specifically focused on uncoupled, 2LP-mode MCFs within the standard 125 μm cladding diameter limit. A numerical simulation study is presented in this chapter, followed by a comparison with the results of previous experimental and simulation studies.

We briefly examine the SCC, calculated as the product of the number of cores and modes. Figure 15 depicts the correlation between SSC and XT in both single-mode and 2LP-mode MCFs, with XT values pertaining to the highest-order modes in adjacent cores. It is noteworthy that utilizing the 2LP-mode results in a significant threefold increase in SCC compared to the single-mode Hetero-MCF. Importantly, the increase in SCC can be realized with only minor changes in XT, which highlights the potential advantages of using 2LP-mode to increase the capacity of optical communication systems.

Chapter 4. Characteristics of 2LP-mode Hetero-SI-MCFs with double-cladding structure

It is difficult to expand the number of cores with enough low XT with 8-core fibers having XTs of −35 dB/km in Chapter 3. A reduction in XT requires an increase in the distance between cores. The core H (with a higher refractive index) can be moved to a more outward position in this case to increase the distance between the cores. Due to the moving of the core, parameters such as the core radius, refractive index, and mode losses will also be increased to meet mode transmission requirements (e.g., *BL* limitations). A double-cladding structure was proposed as a solution to that problem. In Ref. [16], an uncoupled-type 2LP-mode homogeneous 4-core fiber with the double-cladding layer has been reported, which achieved a relative core multiplicity factor (RCMF) of more than 10 for the first time among MCFs with a 125-μm CD while keeping the feasible XT and an effective area (A_{eff}).

To further reduce the XT, the use of heterogeneous cores is effective. In addition, by using the two-ring layout for Hetero-MCFs, as I mentioned in Chapter 3, a high refractive index external cladding allows higher-order modes in the core H to be more easily cutoff, ensuring the transmission of the required modes by suppressing higher-order modes in the core H when they have moved outside the cladding. It is expected that the number of cores in 2LP-mode MCF with a 125-μm CD can be increased while keeping low XT.

4.1 Diagram of the double-cladding structure

Fig. 16 (a) shows the double-cladding structure Hetero-SI-MCFs with a two-ring core layout we used in this paper. For this structure, the outer cladding (shown by the orange region) with the thickness of t_{oc} is added to the outside of the inner cladding. When the outer cladding thickness $t_{\mathrm{oc}} = 0$, the structure is the same as Fig. 8 (a). Also, the diameter of the whole fiber is kept to 125 μm even when the outer cladding is used.

In this study, we assume a step-index profile of double-cladding, as depicted in Fig. 16 (b), where n_{core} (core H and core L) and n_{clad} represent the refractive indices of the core and inner cladding, respectively. And the n_{oc} denotes the refractive index in the outer cladding. The value of n_{clad} is set to 1.45 to represent the refractive index of pure silica, while the refractive index outside of the cladding is set to 1.486, which corresponds to the coating material [31]. The parameters are the same as described in subsection *3.1*, except for t_{oc}.

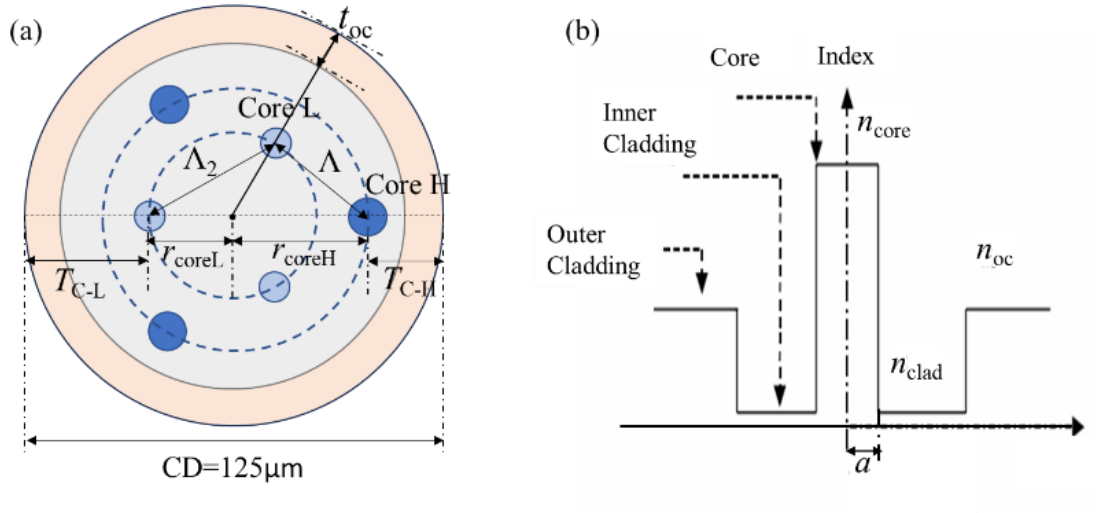

Fig. 16. Schematics of the (a) fiber cross sections and (b) refractive index profile of core.

4.2 Parameter for outer cladding for C-band

This section outlines the process involved in designing MCFs with a double-cladding structure. Compared with the traditional single-cladding MCFs, a double-cladding fiber has an additional outer cladding layer, which is defined by the width t_{oc} and relative refractive index difference Δ_{oc} (= $(n_{oc}^2 - n_{clad}^2)/2n_{oc}^2$) between the inner cladding and the outer cladding. It was shown that $T_{C\text{-}H}$ = 29 μm is the minimum value of MCFs at t_{oc} = 0 μm (single-cladding two-ring core layout MCFs introduced in Chapter 3), we anticipate that the minimum value of T_C will be further reduced by properly adding the outer cladding layer. A smaller $T_{C\text{-}H}$ will increase

the size of the *ECR* causing a larger difference in the effective refractive indices of adjacent cores, leading to smaller XT.

To evaluate the size of *ECR*, which is shown in Fig. 10, we define the effective refractive index (n_{eff}) difference of LP_{11} mode between the upper cutoff limit (n_{eff} at the cutoff limit) and the lower *EL* limit (n_{eff} at the *EL* limit) of *ECR* as Δn_{ECR}. If $\Delta n_{ECR} < 0$, the design region determined by the cutoff and *EL* in Fig. 10, such as the region between points *N* and *O*, disappears. Therefore $\Delta n_{ECR} > 0$ is necessary for fiber design. Fig. 17 (a) shows the n_{eff} value for the upper and lower *ECR* limits of LP_{11} mode for single-cladding and double-cladding (Δ_{oc} = 0.34%, t_{oc} = 14 μm) MCFs. And Fig. 17 (b) shows the relationship between Δn_{ECR} and T_C. It can be found that compared with the single-cladding MCF of the black line, fluctuations of Δn_{ECR} can be seen in the double-cladding MCF in Fig. 17 (b) when T_C = 29 to 31 μm.

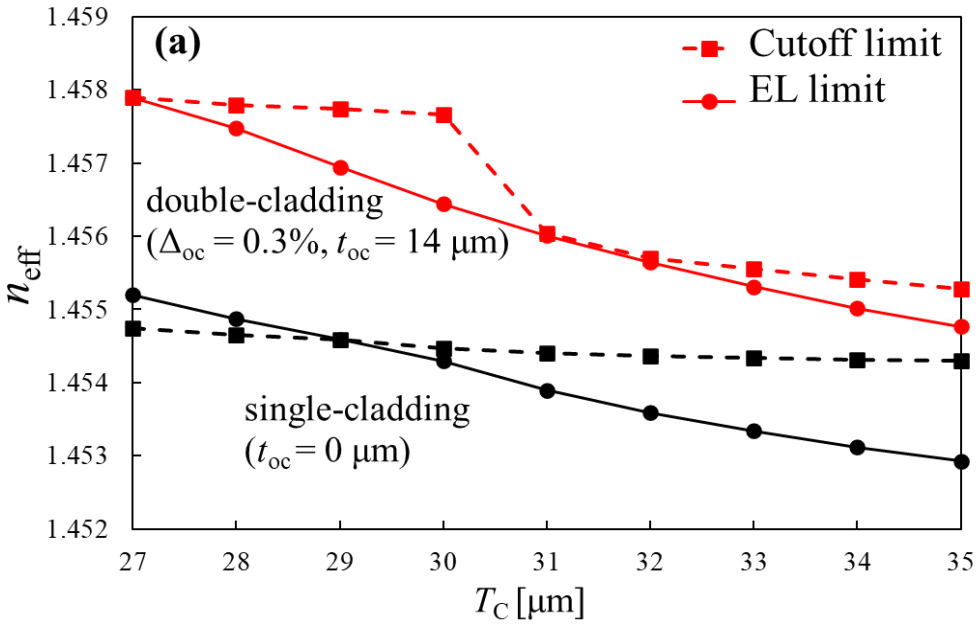

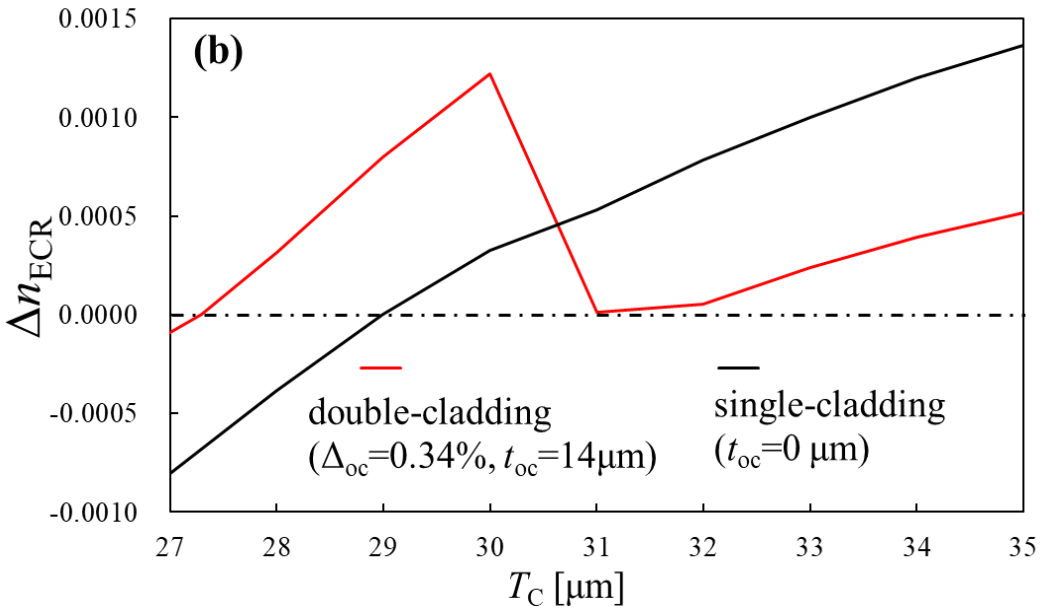

Fig. 17. n_{eff} and Δn_{ECR} for LP_{11} modes between ECR limit points in single- and double-cladding Hetero-MCF as a function of T_C (T_C = 27.3-35 μm). (a) n_{eff} as a function of T_C. (b) Δn_{ECR} as a function of T_C.

To explain why the fluctuation occurred, we have selected some sets of core parameters (a, Δ) of double-cladding MCF by maintaining A_{eff} = 80 μm^2. Then, we calculated the *BL* of LP_{21} mode separately at T_C = 29 to 31 μm using the core parameters obtained from these points, and the *BL* as a function of core radius a is shown in Fig. 18. The star symbols represent the cutoff limit points of *ECR* at T_C = 29 to 31 μm with different color, respectively. The horizontal black dashed lines represent the cutoff limit of the *ECR* conditions. From Fig. 18 following features can be extracted. First, for smaller T_C, the *BL* becomes large due to the short distance to the outer cladding. Second, for smaller values of a (at the same time, Δ is reduced to maintain A_{eff}), the *BL* also becomes large due to weaker confinement. Third, there seems to be a plateau in the middle range of a. The last point can be explained by the coupling between the core and the cladding modes. The coupling between the two modes can be clearly observed by the electric field distributions, which are shown in Fig. 18 such as points *M* and *N*. The coupling causes the *BL* modification and makes a plateau as the region between points *P* and *Q*. In Fig. 18, for T_C = 30 μm, the cutoff limit is at the red star symbol, however, for T_C = 31 μm, due to the reduction of *BL*, the cutoff limit moves to the blue star symbol. Therefore, the cutoff condition of the LP_{21} mode (*BL* > 1 dB/m) is changed significantly for the core

parameters at T_C = 31 μm, like the distance between the red and blue star symbols in Fig. 18. It leads to a significant change in n_{eff} of the cutoff limit core like the dashed red line in Fig. 17 (a) and a decrease in Δn_{ECR} which shown in Fig. 17 (b) by red line as well.

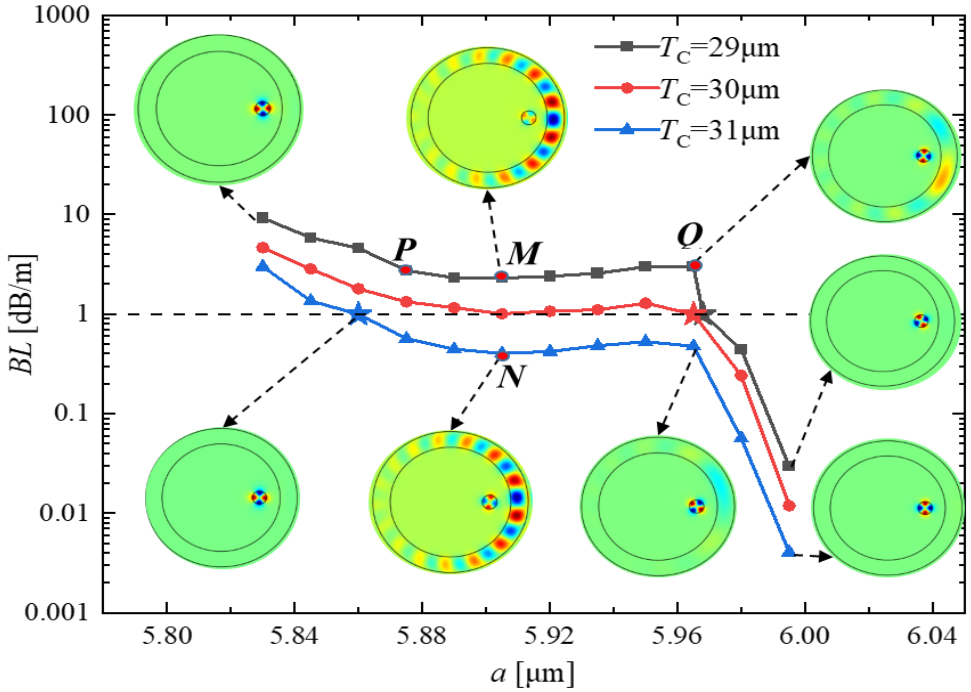

Fig. 18. The *BL* distribution of LP_{21} mode, which uses the core parameters maintaining A_{eff} = 80 μm^2, where T_C = 29, 30, and 31 μm.

For our previously proposed two-ring core layout Hetero-MCF, we need to find a set of core parameters (a, Δ) that can satisfy both the LP_{21} mode cutoff condition and the LP_{11} mode transmission condition. That means Δn_{ECR} = 0. To determine the proper fiber parameters, Fig. 19 shows the distribution of t_{oc} vs. Δ_{oc} for Δn_{ECR} = 0, where T_C decreases gradually from 28 μm to 27 μm.

We used $t_{oc} = T_C - 3a$ as in [16], and the range of T_C in a single-cladding Hetero-MCF is 29-36 μm, and the fiber radius a is 5.2-5.7 μm according to Chapter 3. The core radius a increases, and T_C decreases with the use of outer cladding. The minimum value of T_C is close to 27 μm and the maximum value of a is close to 6 μm. So, according to the previously mentioned relationship of t_{oc}, T_C, and a ($t_{oc} = T_C - 3a$), we set the range of t_{oc} calculation to 8-18 μm. However, during the calculation, we observed that when T_C < 27.5 μm and t_{oc} values are 8 and 9 μm, there are no

regions for $\Delta n_{ECR} > 0$. So, in Fig. 19, we present the results of the calculations within the range of t_{oc} values from 10 to 18 μm.

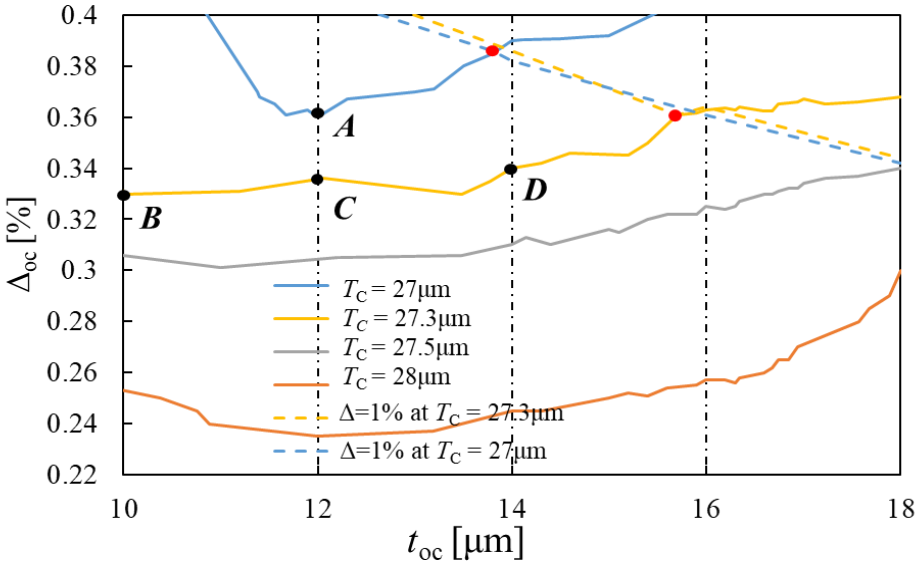

Fig. 19. Relationship between t_{oc} and Δ_{oc} for Δn_{ECR}=0, where T_C = 27, 27.3, 27.5, 28 μm.

However, during the calculation, we observed that when T_C < 27.5 μm and t_{oc} values are 8 and 9 μm, there are no regions for $\Delta n_{ECR} > 0$. So, in Fig. 19, we present the results of the calculations within the range of t_{oc} values from 10 to 18 μm. The upper region of the colored solid line represents $\Delta n_{ECR} > 0$, and the below is the opposite. As can be seen from Fig. 19, T_C can also continue to decrease with further increase in Δ_{oc}, also the core parameters (a, Δ) are increasing. Considering the loss and fabrication issues of MCFs, the core parameters should be limited, and we limit the maximum value of core Δ to 1% in this paper. Although we assumed a core relative refractive index difference of Δ < 1%, there will be other possibilities for fiber structures for further study. The colored dashed lines in Fig. 19 represent the Δ limit for each T_C value with the same color. The red points indicate Δ = 1% and $\Delta n_{ECR} = 0$, while the region below the dashed line represents the core Δ < 1%. When T_C > 27.5 μm, all Δ_{oc} and t_{oc} values (range shown in Fig. 19) satisfy the condition Δ < 1%. To minimize XT, we need to determine the smallest possible T_C value. Therefore, we extracted the points *A*, *B*, *C*, and *D* in Fig. 19, and presented their parameters in Table. IV. Hereafter, we consider these four structures. The

distributions of Δn_{ECR} as a function of T_C for these structures are shown in Fig. 20. And we can find similar fluctuations as Fig. 17 (b).

Table IV. Core parameters extracted from Fig. 16, which satisfy the condition $\Delta < 1\%$

Structure	T_C [μm]	a [μm]	Δ [%]	Δ_{oc} [%]	t_{oc} [μm]
A	27	5.98	0.96	0.36	12
B	27.3	5.92	0.89	0.33	10
C	27.3	5.95	0.93	0.34	12
D	27.3	5.99	0.96	0.34	14

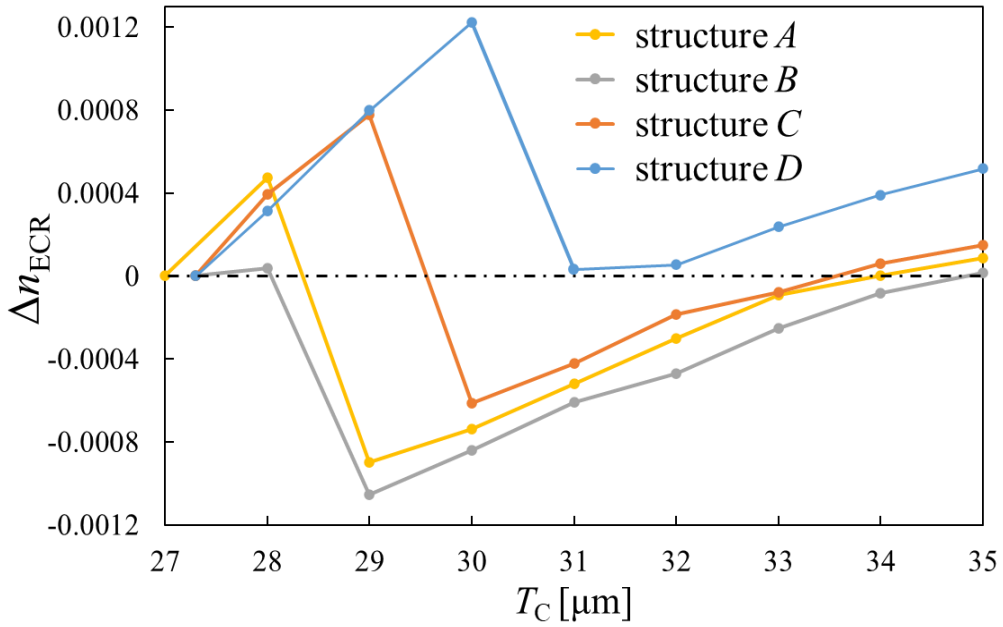

Fig.20. Δn_{ECR} for LP_{11} modes between ECR limit points in double-cladding Hetero-2LP-MCF as a function of T_C for structures *A*, *B*, *C*, and *D*.

As mentioned before, $\Delta n_{ECR} < 0$ means that there is not a possible candidate of the core parameter (a and Δ) satisfying two *BL* conditions, whereas, for structure *D* ($\Delta_{oc} = 0.34\%$ and $t_{oc} = 14$ μm), Δn_{ECR} becomes positive for all $T_C \geq 27.3$ μm as shown in Fig. 20 like the blue line, which means that $T_{C\text{-}H}$ can be reduced. As the previously mentioned XT equation shows, we should choose the fiber parameters with larger differences to obtain a lower XT. Therefore, we choose structure *D* and calculate XT between adjacent cores in the next section for all $T_{C\text{-}L}$ values.

As previously indicated, when $\Delta n_{ECR} < 0$, it implies that there is no viable candidate for core parameters (a and Δ) that satisfies both *BL* conditions. However, in the case of structure *D*, characterized by $\Delta_{oc} = 0.34\%$ and $t_{oc} = 14$ μm, Δn_{ECR} becomes positive for all $T_C \geq 27.3$ μm, as depicted by the blue line in Fig. 20. This signifies that $T_{C\text{-}H}$ can be reduced.

Given the XT equation discussed earlier, it is evident that selecting fiber parameters with larger differences is conducive to achieving lower inter-core XT. Hence, we opt for structure *D* and proceed to calculate XT between adjacent cores in the subsequent section for all $T_{C\text{-}L}$ values. This strategic choice aligns with the overarching objective of minimizing XT in the design process, underscoring the importance of careful parameter selection in optimizing the performance characteristics of the MCF structure.

4.3 XT simulation of 2LP-mode Hetero-SI-MCFs with double-cladding

Same as Fig. 3, we generated a condensed *BL* distribution that highlights only the upper and lower limits of the *ECR* with the parameters of structure *D* ($\Delta_{oc} = 0.34\%$ and $t_{oc} = 14$ μm) in Fig. 21 and suggests that the possible upper limit of *ECR* (the parameter of core H) can be obtained around the cross point for $T_C = 27.3$ μm. Same as the single-cladding Hetero-MCFs with two-ring core layout, to achieve a larger $\Delta\beta_{pq}$ and a lower averaged power-coupling coefficient $\bar{h}_{pq}$, we need to fix $T_{C\text{-}H}$ and vary the parameter of core L by increasing $T_{C\text{-}L}$ from the value of $T_{C\text{-}H}$ to 35 μm. Meanwhile, fabrication errors can also occur during the fiber production and manufacturing process in the core radius a and core Δ, so we also evaluate a parameter of core radius a about 0.01 μm inside the design area due to manufacturing errors.

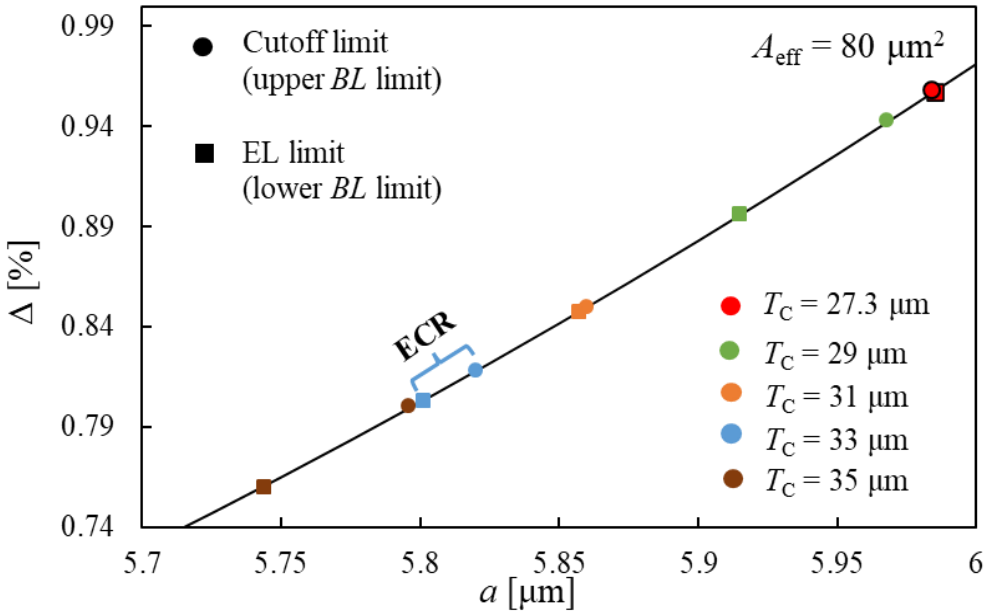

Fig. 21. The core parameters (core radius a and Δ) and their relationship of cutoff limit, EL limit, and A_{eff} at λ = 1550 nm, where T_C = 27.3, 29, 31, 33, and 35 μm.

Figure 22 (a) shows the comparison of XT for LP_{11} mode ($XT_{11\text{-}11}$) between the Hetero-MCFs with the single-cladding mentioned in Chapter 3 and double-cladding layout, where N = 6, λ = 1550 nm, d = 1 m, and $T_{C\text{-}H}$ = 27.3 μm. $XT_{sc,\,dc}$ represents the XT value of single-cladding and double-cladding, respectively. 'H-L' denotes the XT between adjacent cores of core H and core L, and 'L-L' denotes the XT between nearest cores L. Furthermore, we also investigate the case of N = 8 in Fig. 22 (b). As mentioned before, error bars indicate the XT errors due to the core radius variations about 0.01 μm inside the design area. As we can see, for all $T_{C\text{-}L}$, XTs of the double-cladding 6- and 8-core fiber are improved compared with those of the single-cladding layout. Compared with our previous study of single-cladding 6- and 8-core Hetero-MCFs in Chapter 3, the XT of the 8-core MCF was optimized by adding an outer cladding, so we increased the number of cores and wanted to confirm whether the 10-core fiber could also achieve an accepted XT value with the same fiber parameters. The results of the XT calculations of 10-core MCF for each $T_{C\text{-}L}$ are shown in Fig. 22 (c) for structure D ($T_{C\text{-}H}$ = 27.3 μm, Δ_{oc} = 0.34% and t_{oc} = 14 μm).

We can observe that the XT distribution between the 6-, 8- and 10-core Hetero-MCFs does not distribute monotonically. When $T_{C\text{-}L}$ equals 27.3 μm for each fiber

because the R_{pk} of Hetero-MCFs is larger than 140 mm, XT is a relatively large value of the R_b-dominant region which is shown in Fig. 1. When $T_{C\text{-}L}$ reaches 28 μm, the R_{pk} of Hetero-MCFs is smaller than 140 mm, so the XT deceases into a low value of the *d*-dominant region like Fig. 1. Due to the effect of inter-core distance, XT increases with $T_{C\text{-}L}$ for 6- and 8-core fiber. However, the effect of inter-core distance on XT is smaller than the difference between adjacent core parameters (*a*, Δ) of 10-core fiber, so the XT of 10-core fiber will continue to decrease like Fig. 22 (c).

For the 6-core double-cladding layout MCF, the minimum $XT_{11\text{-}11}$ of −97.9 dB/km for adjacent cores can be obtained with structure *D* ($T_{C\text{-}H}$ = 27.3 μm, Δ_{oc} = 0.34% and t_{oc} = 14 μm) with $T_{C\text{-}L}$ = 29 μm, indicating the improvement of 46.7 dB/km compared with the single-cladding layout. The minimum $XT_{11\text{-}11}$ for 8-core double-cladding layouts MCF is −60.4 dB/km at $T_{C\text{-}L}$ = 30 μm for structure *D* ($T_{C\text{-}H}$ = 27.3 μm, Δ_{oc} = 0.34% and t_{oc} = 14 μm), indicating an improvement of 24.5 dB/km compared with the single-cladding layout. And the lowest XT of 10-core MCF reaches −35.5 dB/km. This also means that with the current proposed double-cladding two-ring core layout fiber structure, the 8-core fiber is the one with the highest number of cores while maintaining the XT value under −50 dB/km.

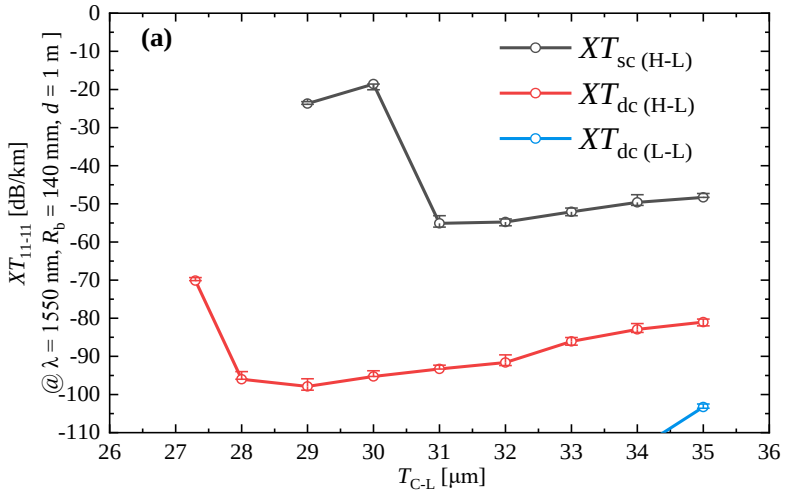

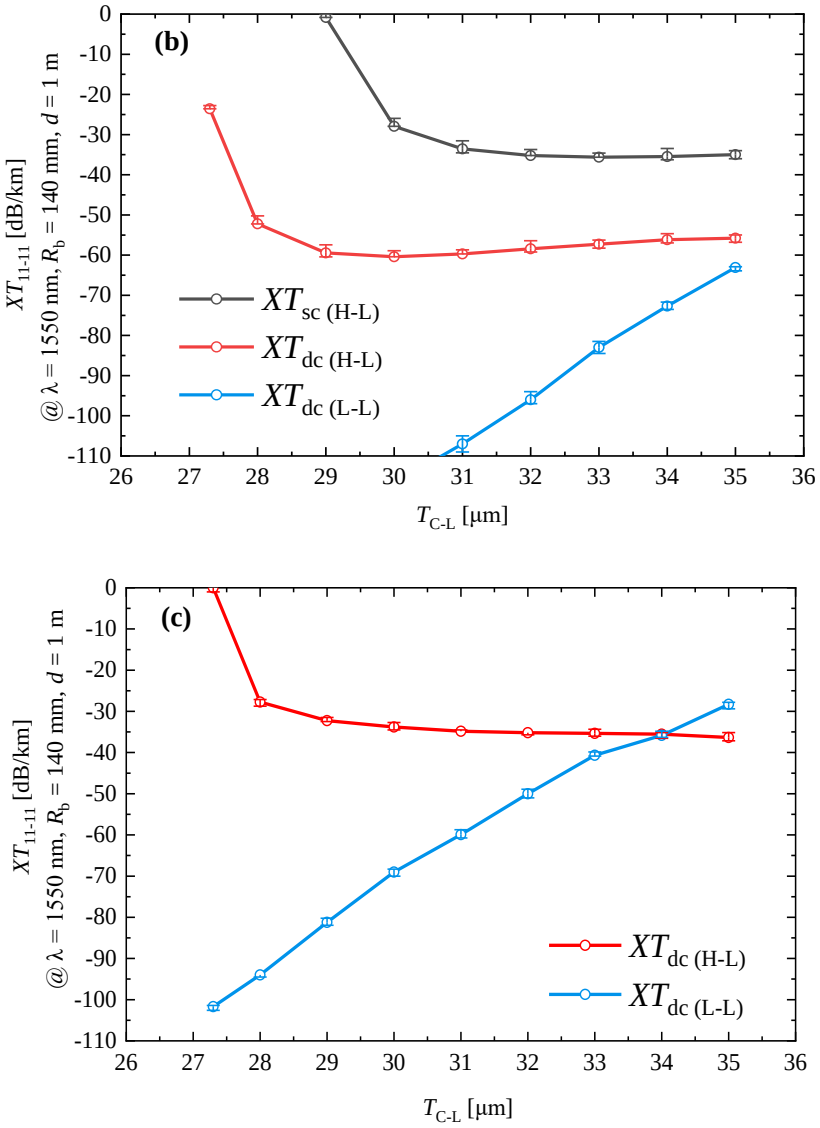

Fig. 22. Comparison of characteristics between the Hetero-MCFs with the single- cladding and double-cladding layer, where N = 6, 8 and 10, and $T_{C\text{-}H}$ = 27.3 μm.

When the inter-core XT is maintained at sufficiently low levels, the potential transmission length (L_{max}) may be constrained by the effects of the differential mode delay (DMD). Focusing solely on the impact of XT on L_{max}, Figure 23 provides a comparative analysis of L_{max} for Hetero-MCFs with different signal formats. The comparison specifically corresponds to $XT_{11\text{-}11}$ for adjacent cores of structure *D*, as illustrated in Figures 22 (b) and (c), with core numbers N equal to 8 and 10.

For the 8-core fiber, the L_{max} for 64QAM is observed to reach approximately 700 km, showcasing the potential for extended transmission distances. On the other hand, the 10-core fiber exhibits an L_{max} of about 90 km for QPSK. These findings

underscore the influence of inter-core XT on the achievable transmission lengths for various signal formats in the context of Hetero-MCFs.

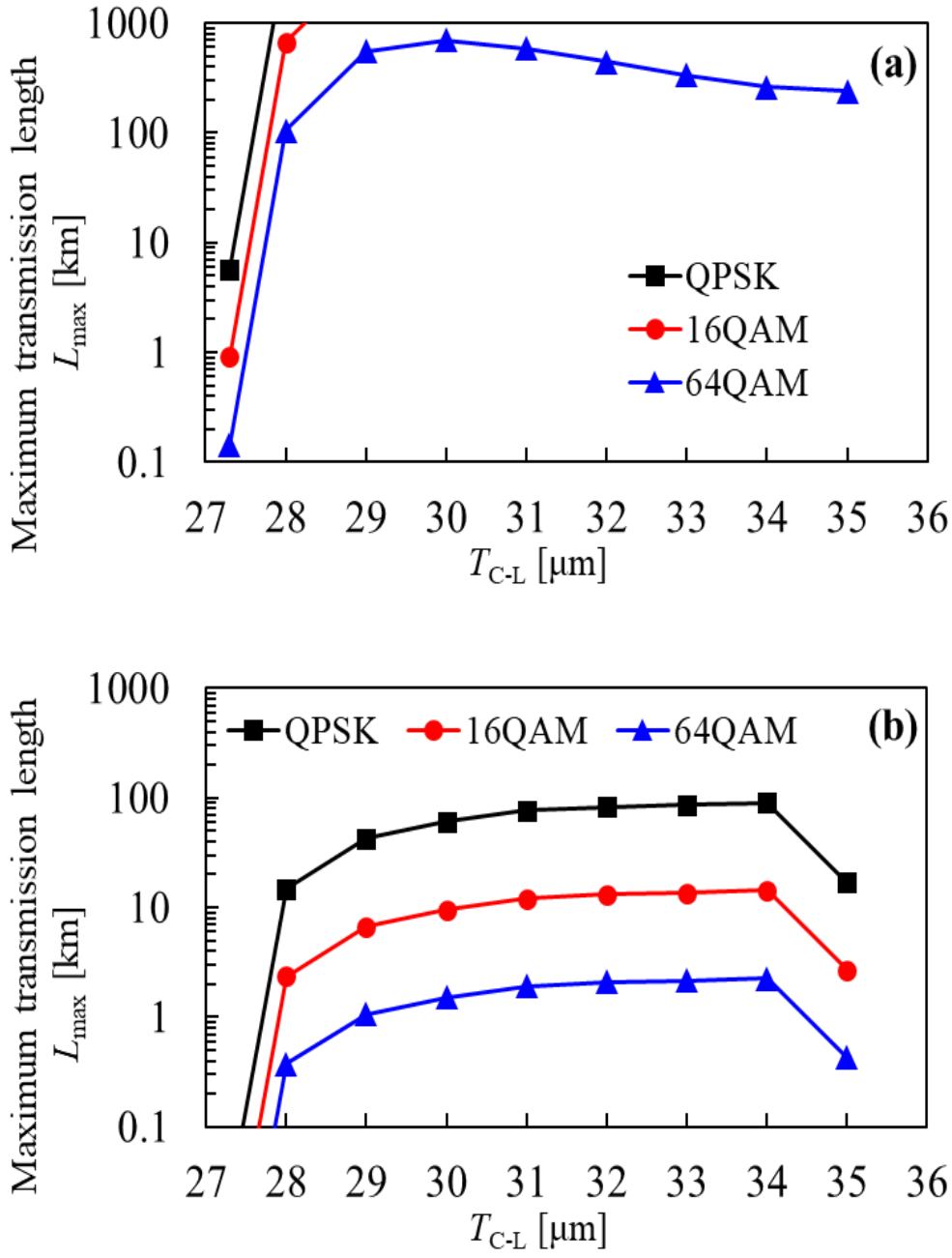

Fig. 23. Comparison of transmission length between the different format signals for Hetero-MCFs with the double-cladding layer: (a) N = 8, and (b) N = 10, where parameters are the same as Fig. 22 (b) and (c).

4.4 Conclusion

By employing the innovative double-cladding structure, the study demonstrates that the manipulation of the outer cladding thickness in MCFs provides a mechanism to expand the core pitch of individual cores. Through the implementation of a simple SI profile, this structural enhancement proves instrumental in realizing 10-core fibers with a feasible level of inter-core XT.

The cross-sectional views of the specifically designed and modified 6-core, 8-core, and 10-core Hetero-SI-MCFs intended for the C-band are vividly illustrated in Figure 24 (a), (b), and (c), respectively. These visual representations offer valuable insights into the spatial arrangement and distribution of cores within the fiber structure. In each case, cores characterized by a higher core refractive index are strategically allocated within the circle with a specified outer cladding thickness ($T_{C\text{-}H}$). Simultaneously, cores with a lower core refractive index are judiciously assigned to another circle characterized by a different outer cladding thickness ($T_{C\text{-}L}$). The precise values of $T_{C\text{-}L}$ are adjusted to optimize the performance of the respective 6-core, 8-core, and 10-core fibers, ensuring the desired characteristics and XT levels are achieved for each configuration.

This detailed expansion provides a comprehensive overview of the structural modifications and design considerations employed in achieving 6-, 8-, and 10-core Hetero-SI-MCFs for optimal performance within the C-band. The nuanced adjustments in outer cladding thickness, guided by a simple SI profile, showcase the potential for tailoring fiber structures to meet specific application requirements while adhering to standardized cladding diameters. This information contributes to the broader understanding of fiber design possibilities and opens avenues for further optimizations in the field of multi-core fiber technologies.

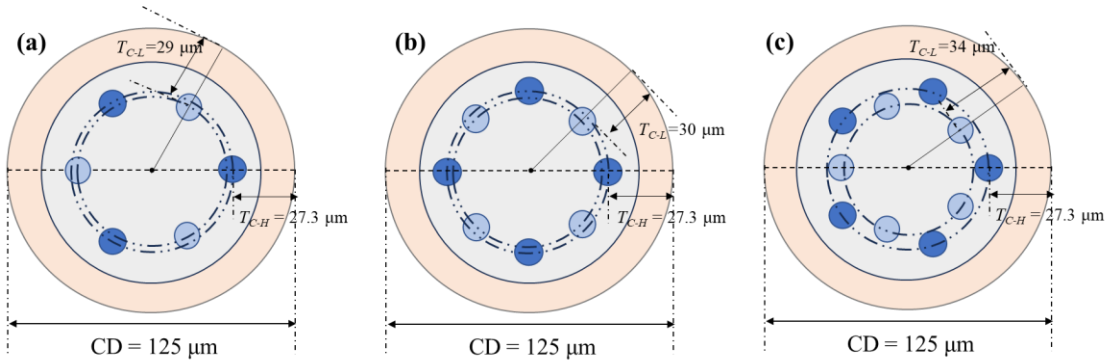

Fig. 24. Cross sections of the designed Hetero-SI-MCFs with double-cladding structure for C-band. (a) 6-core fiber. (b) 8-core fiber. (c) 10-core fiber.

The core parameters employed in the design of Hetero-SI-MCFs featuring the innovative double-cladding structure optimized for the C-band are meticulously detailed in Table V. Core H, distinctly marked by a red dot in Figure 21, designates the core with a higher core refractive index. Among the fiber configurations with different core numbers, core L serves as the core with the lower refractive index.

Table VI succinctly encapsulates the key parameters of the designed Hetero-SI-MCFs, showcasing the nuances of the double-cladding structure tailored specifically for optimal performance within the C-band. A detailed description of each fiber's core characteristics, refractive index, and other essential factors impacting the fiber's behavior in C-band applications can be gained by knowing these parameters.

Table V. Core parameters for designed Hetero-MCFs

T_C [μm]	a [μm]	Δ [%]	A_{eff} [μm^2]	Core name
27.3	5.98	0.96	80.1	Core H
29	5.93	0.90	79.9	Core L (N = 6)
30	5.89	0.86	80.1	Core L (N = 8)
34	5.77	0.76	80.0	Core L (N = 10)

Table VI. Fiber parameters of the designed Hetero-MCFs

N	$T_{C\text{-}H}$ [μm]	$T_{C\text{-}L}$ [μm]	Λ [μm]	Λ_2 [μm]	$XT_{11\text{-}11}$ [dB/km]
6	27.3	29	34.5	58.0	−97.9
8	27.3	30	26.0	45.9	−60.4
10	27.3	34	20.7	33.5	−35.5

Figures 25 (a), (b), and (c) illustrate the variations in the calculated nearest inter-core XT between adjacent non-identical cores concerning the bending radius (R_b) for the specifically designed 6-, 8-, and 10-core fibers, respectively. The XT calculations are performed at a wavelength (λ) of 1550 nm, with the correlation length (d) assumed to be 0.1 m, 1 m, and 10 m, respectively.

In both MCFs, the observed trend reveals an increase in XT as the R_b increases within the R_b-dominant region. However, a notable shift occurs when transitioning into the d-dominant region, where XT undergoes a decrease, reaching an ultra-low value. Remarkably, in this region, XT becomes insensitive to further variations in the R_b. This nuanced analysis provides a comprehensive understanding of how bending radius influences inter-core XT in the designed MCF under different correlation length scenarios, offering valuable insights for optimizing their performance in practical optical communication systems.

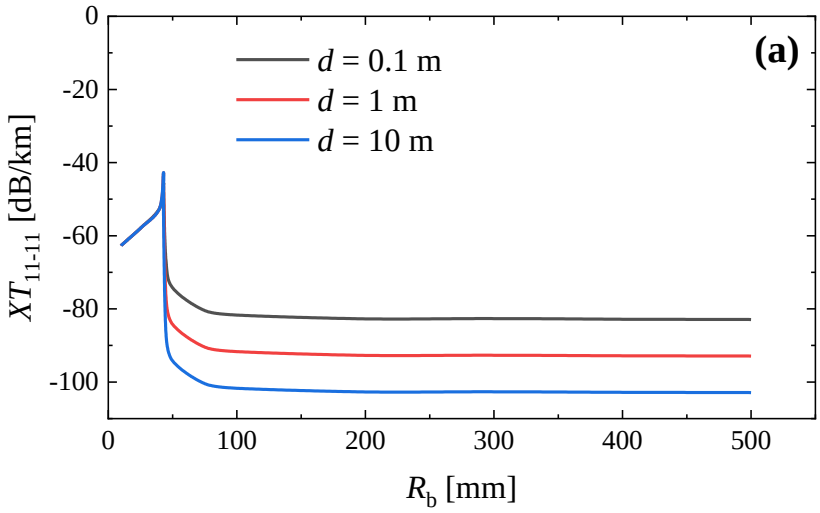

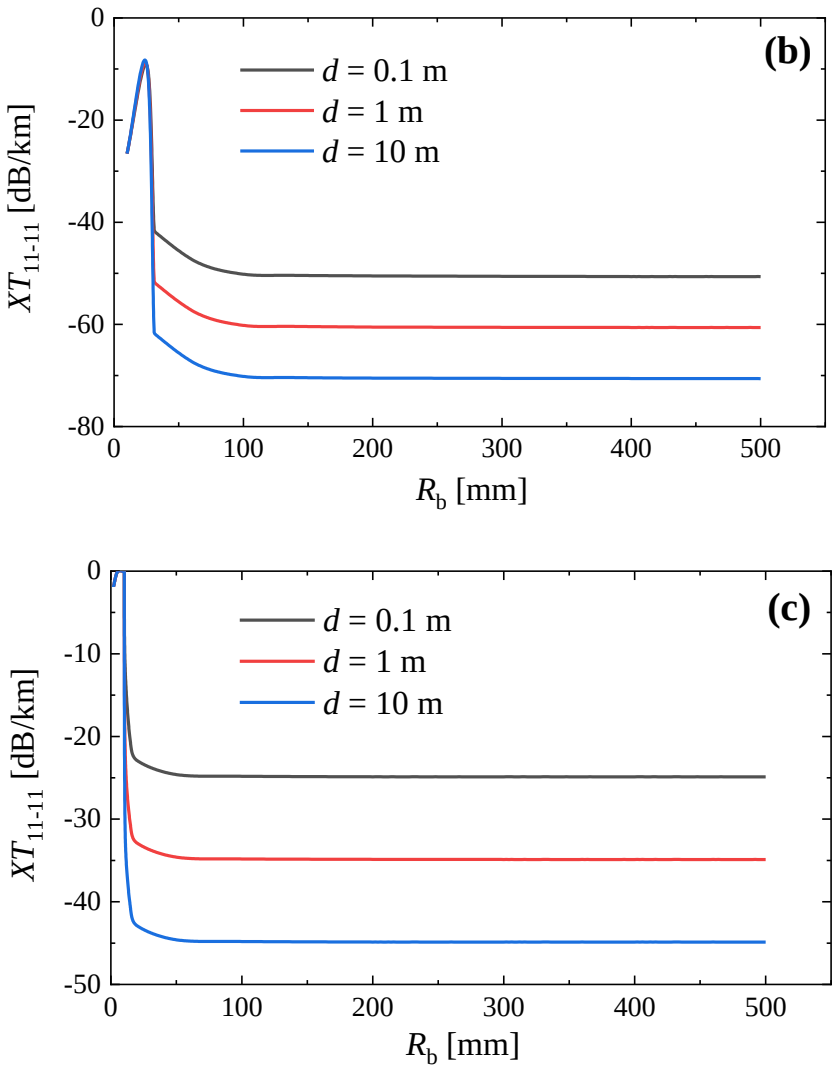

Fig. 25. $XT_{11\text{-}11}$ of the double-cladding Hetero-MCF as a function of R_b, where λ = 1550 nm. (a) 6-core fiber. (b) 8-core fiber. (c) 10-core fiber.

In the evaluation of inter-core XT distribution for the LP_{11} mode within the C-band range (1530-1565 nm), we present the results for 6-, 8-, and 10-core MCFs employing a two-ring core layout and a double-cladding structure in Figure 26. The depicted XT distribution provides insights into the performance of these Hetero-MCFs across the specified wavelength range.

Furthermore, we highlight the worst-case XT values for the 6- and 8-core fibers, both of which demonstrate remarkably low XT values. This observation suggests excellent performance within the C-band, underscoring the efficacy of the designed MCF configuration. The core parameters utilized for these evaluations align with

those detailed in Table VI, emphasizing the practicality and applicability of the proposed design for C-band applications in optical communication systems.

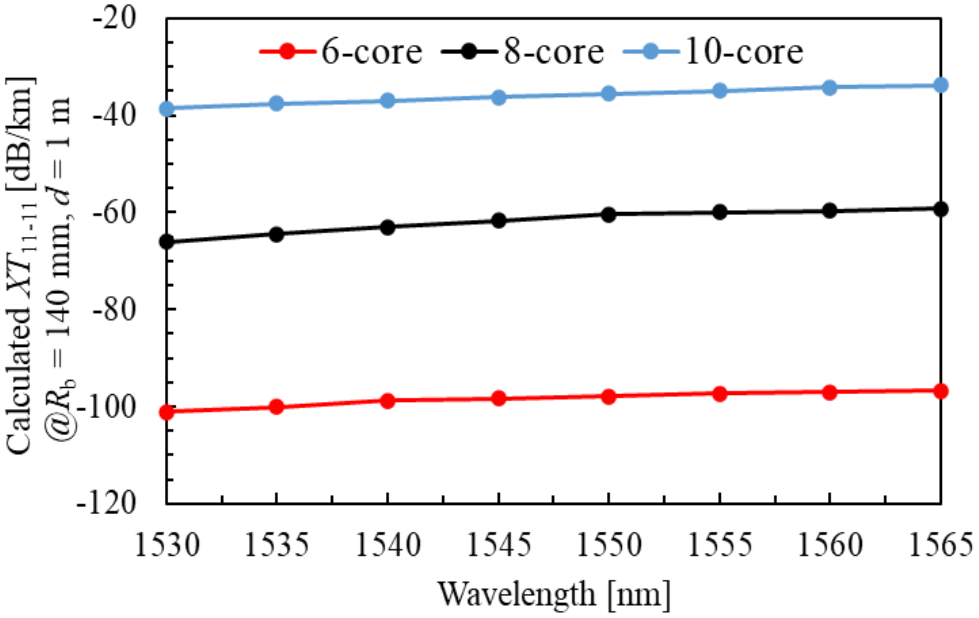

Fig. 26. Comparison of XT between the Hetero-MCFs with double-cladding for C-band, where N = 6, 8 and 10, while keeping the other parameters the same as Table VI.

In a succinct analysis, we turn our attention to the SCC, a parameter calculated as the product of the number of cores and modes within the MCF. The examination of SCC becomes particularly insightful in understanding the fiber's overall capacity and performance. Figure 27 visually presents the correlation between SCC and inter-core XT for both single-cladding and double-cladding 2LP-mode MCFs, focusing on XT values associated with the highest-order modes in adjacent cores.

The observation gleaned from Figure 27 is pivotal: in comparison to single-cladding Hetero-MCFs, the incorporation of a double-cladding structure manifests as a notable enhancement in XT while maintaining the same SCC value. This finding underscores the impact of cladding design on the trade-off between SCC and inter-core XT, offering valuable insights into the potential advantages and considerations associated with the use of double-cladding in 2LP-mode MCFs.

This brief yet informative analysis contributes to the broader understanding of the interplay between SCC and XT in multi-core fiber designs, particularly when considering different cladding structures. The implications of these findings are instrumental for optimizing MCF configurations to meet specific performance requirements in optical communication systems.

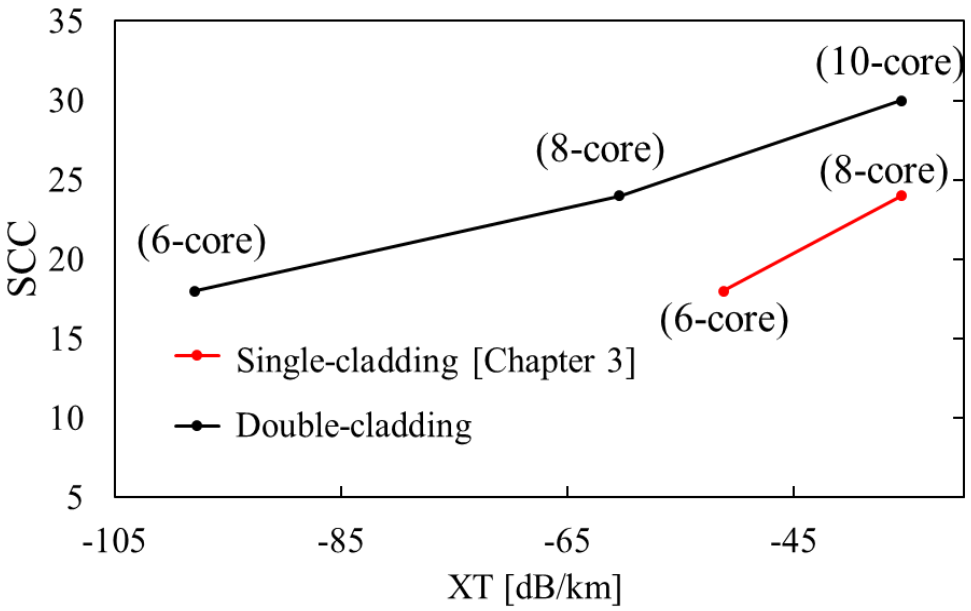

Fig. 27. Comparison of SCC and XT between single-mode and 2LP-mode Hetero MCFs.

Chapter 5. Application of the two-ring core layout on 4LP-mode Hetero-SI-MCFs and C+L-band

5.1 4LP-mode Hetero-SI-MCF with two-ring core layout

In the course of this study, the implementation of a two-ring core layout has led to the successful development of uncoupled-type 2LP-mode Hetero-MCFs featuring 6 and 8 cores, thereby achieving SCC of 18 and 24 within the confines of a 125-μm cladding diameter, as elaborated in Chapter 3. This notable accomplishment is underscored by the ability to maintain commendable XT levels and an effective area (A_{eff}) throughout the design process.

However, a challenge surfaces in the form of the lowest XT value of -35 dB/km for the 8-core fiber, signifying the difficulty in increasing the number of cores while simultaneously keeping XT at low levels. To navigate this challenge and further enhance the SCC without compromising on low XT, the subsequent subsection explores innovative approaches. Here, we introduce a Heterogeneous 4LP-mode MCF, meticulously designed for C-band utilization, accommodating LP_{01}, LP_{11}, $LP_{21,}$ and LP_{02} modes. This novel MCF leverages a thoughtfully devised two-ring core layout, aiming to optimize both performance and efficiency in a synergistic manner.

The cross sections of the 4LP-mode 4- and 6-core Hetero-SI-MCFs with two-ring core layouts are shown in Fig. 28 (a) and (b), respectively.

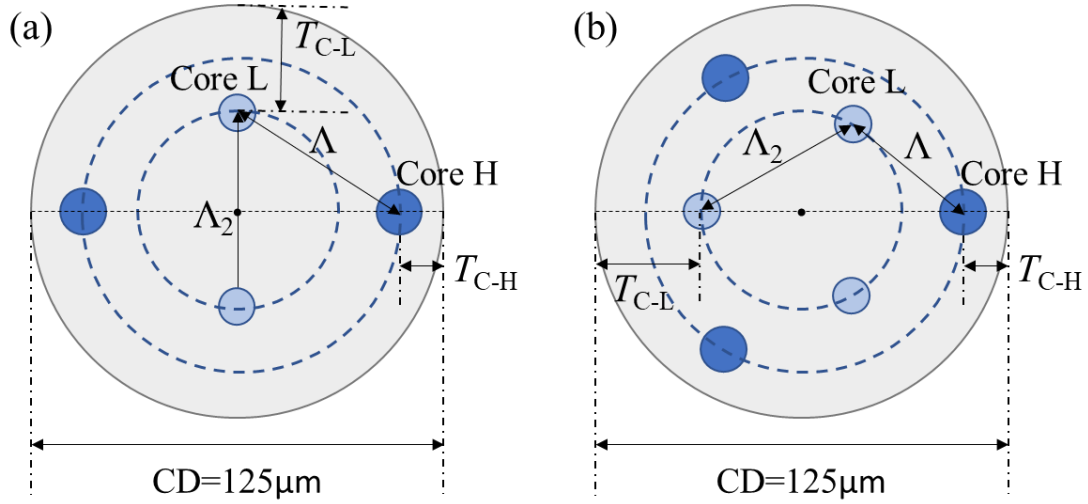

Fig. 28. Schematic of the Hetero-MCFs with two-ring core layout design. (a) Cross-section of the 4-core Hetero-MCFs. (b) Cross-section of the 6-core Hetero-MCFs.

Similar to Figure 3, Fig. 29 illustrates the general approach for selecting core parameters in the context of a 4LP-mode. In this figure, a represents the core radius, Δ is the relative refractive index difference between the core and the cladding, and T_C is the distance between the core and cladding. Figure 29 provides criteria for core selection based on the cutoff *BL* limit of the LP_{31} mode, which should exceed 1 dB/m at a wavelength (λ) of 1530 nm and a R_b of 140 mm. The dashed lines of different colors denote the cutoff *BL* limit for various T_C values.

Similarly, the excess loss (*EL*) limit of the LP_{02} mode is considered, aiming for it to be less than 0.01 dB/km at λ = 1565 nm and R_b = 140 mm. These *EL* limit lines are indicated by solid lines of the same color as the corresponding cutoff *BL* limits for the given T_C value. Additionally, the dot-dashed black line in the figure represents the contour line for an A_{eff} of 80 μm² for the LP_{01} mode at λ = 1550 nm. This comprehensive representation aids in guiding core parameter selection for designing 4LP-mode multicore fibers.

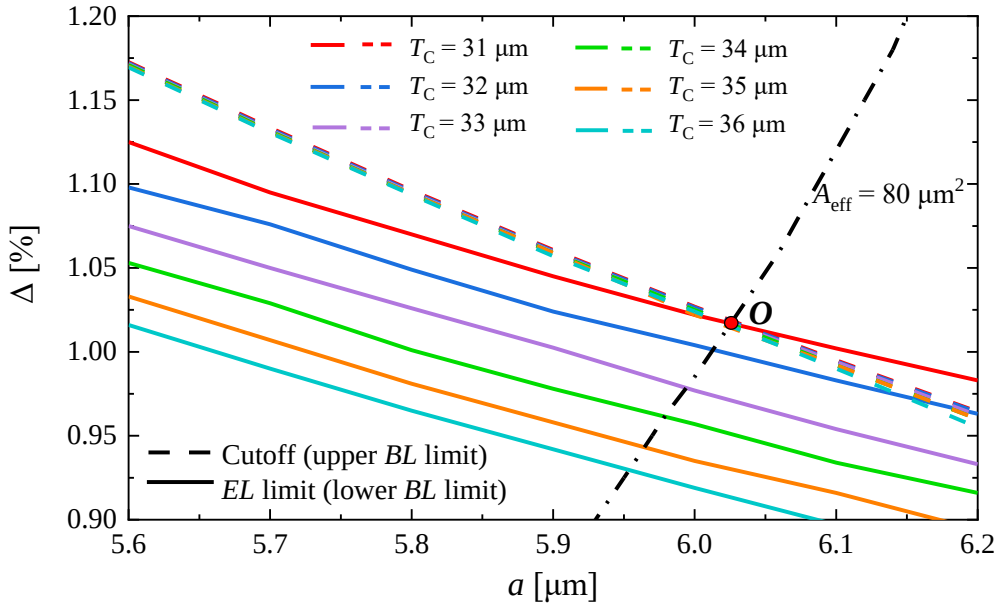

Fig. 29. Relationship between the core parameters and effective indices of 4LP-mode for the C-band.

XT evaluation

Figure 5 highlights that within the 2LP-mode, the inter-core XT between the LP_{11} modes of two cores ($XT_{11\text{-}11}$) attains the highest values compared to other mode combinations. However, as depicted in Figure 30, the effective refractive indices (n_{eff}) of the LP_{21} and LP_{02} modes exhibit close proximity, suggesting the potential for coupling between these two modes. Building upon this insight, Figure 31 further explores and evaluates the XT between the LP_{21} modes in both core H and core L ($XT_{21H\text{-}21L}$), as well as between the LP_{02} mode in core H and the LP_{21} mode in core L ($XT_{02H\text{-}21L}$). The designations $XT_{21H\text{-}02L}$, $XT_{02H\text{-}02L}$, and $XT_{02L\text{-}02L}$ adhere to a consistent nomenclature, providing a detailed representation of the specific modes and cores involved in the inter-core crosstalk assessment.

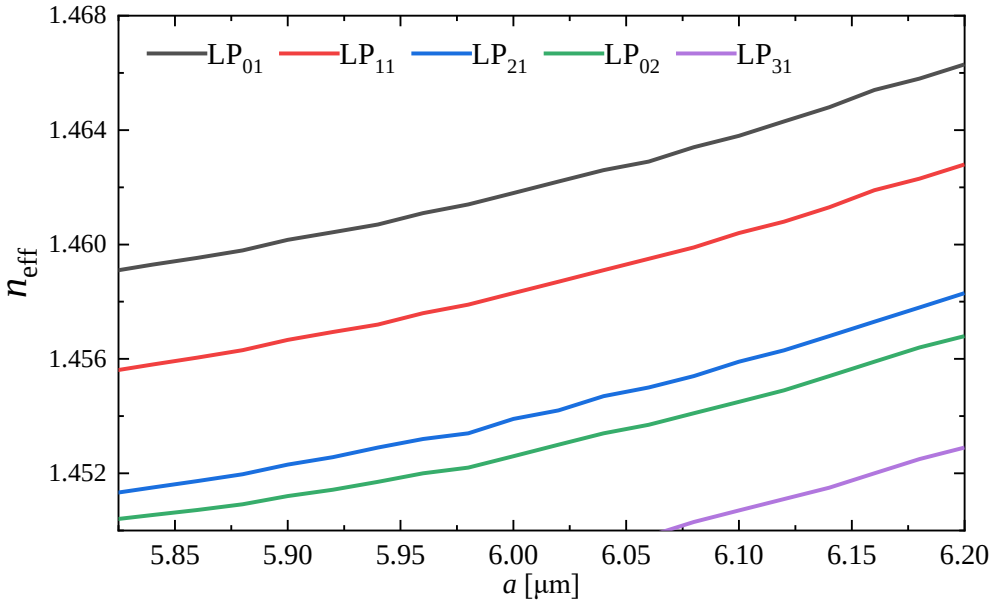

Fig. 30. The n_{eff} distribution of each mode at λ =1565 nm, A_{eff} = 80 μm^2, T_C = 31 μm.

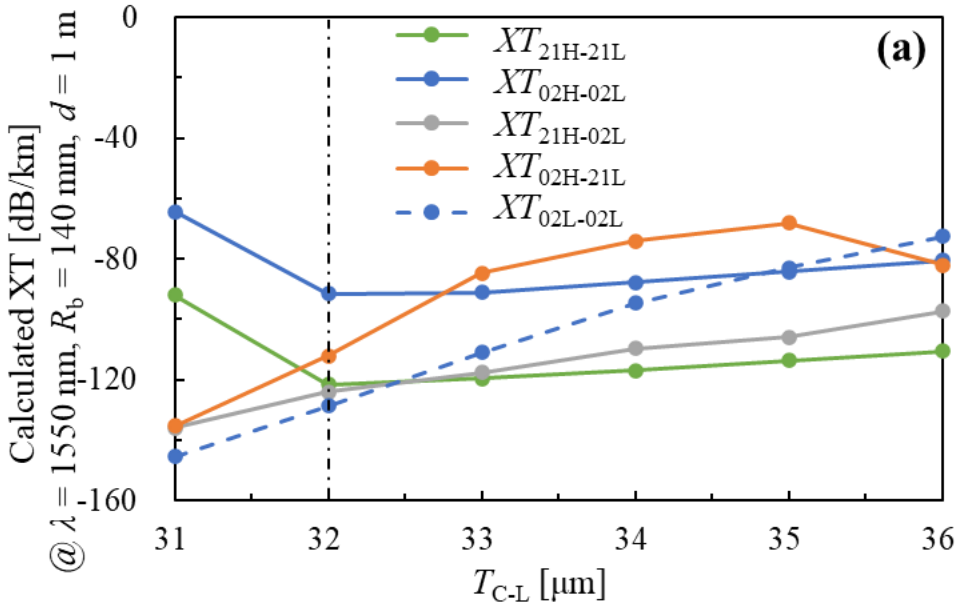

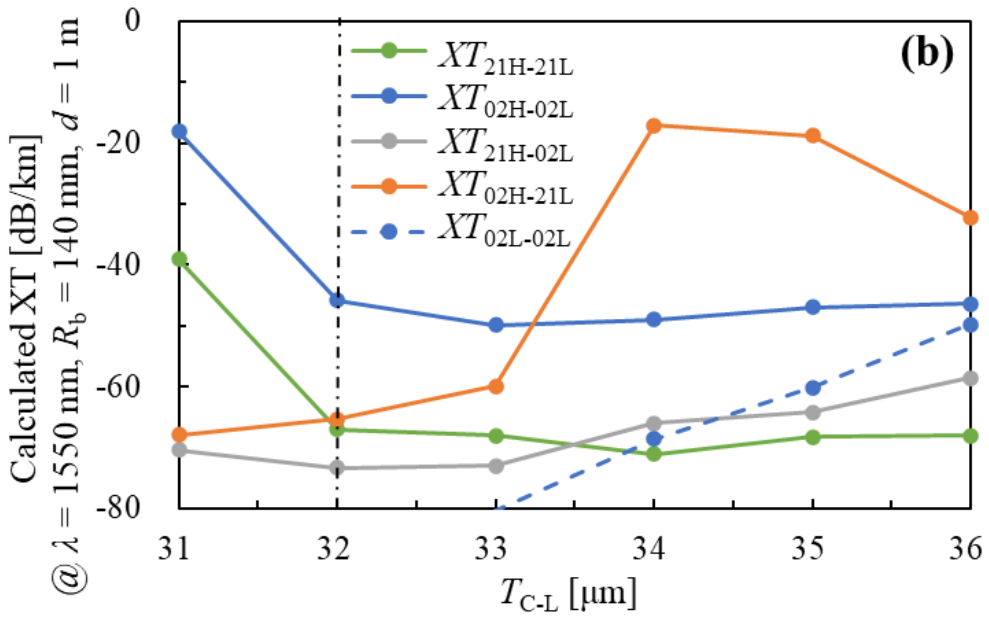

Fig. 31. Calculated XTs between cores H and core L as functions of T_{C-L}. (a) $N = 4$. (b) $N = 6$.

The smallest XT of −91 dB/km can be obtained when T_{C-H} = 31 μm and T_{C-L} = 32 μm where the core number N = 4. This XT value is lower than that in the homogeneous 2LP-4CF, which is −50 dB/km [34]. And −49 dB/km can be obtained when T_{C-H} = 31 μm, T_{C-L} = 33 μm for N = 6. As shown in Fig. 31, when T_{C-L} equals 31 μm, because the R_{pk} of 4LP-MCFs is larger than 140 mm, XT is in the bending-sensitive region, and the value is large. When T_{C-L} reaches 32 μm, the R_{pk} of Hetero-MCFs is smaller than 140 mm, so XT is in the bending-insensitive situation, and the value becomes small [26]. The core pitch Λ between adjacent different cores, as shown in Fig. 28, decreases as the T_{C-L} increases, leading to an increase in XT. According to the XT calculation formulas we used in [27], there is a tradeoff between the parameters that determine the XT value, such as the n_{eff} difference between adjacent cores and mode coupling coefficients, etc. An optimal value can be achieved by optimizing the combination of these parameters, leading to the lowest XT values, shown in Fig. 31, like the black dot-dashed lines. As T_{C-L} increases from T_{C-H}, the n_{eff} difference between the LP_{02} mode in core H and the LP_{21} mode in neighboring core L gradually decreases. This could lead to a stronger mode coupling than the same order modes. As shown in Fig. 31, the coupling occurs between the LP_{21} and LP_{02} modes in certain parameters but not at the lowest XT fiber parameters we have chosen in Fig. 31 (a) and (b) with black dot-dashed lines.

If the XT value is sufficiently low, the transmission length L_{max} may be limited by the differential mode delay (DMD), however, in this paper, we are only considering the effects of XT on L_{max}. Fig. 32 shows the distribution of L_{max} for the 4LP-mode 6-core fiber with each format signal. L_{QPSK} suddenly reduced at $T_{C\text{-}L}$ = 34 μm because the worst XT values used in Eq. (12) are changed from $XT_{02H\text{-}02L}$ to $XT_{02H\text{-}21L}$, as shown in Fig. 31 (b). And the 6-core fiber's L_{QPSK} reaches over 2400 km when $T_{C\text{-}L}$ = 33 μm.

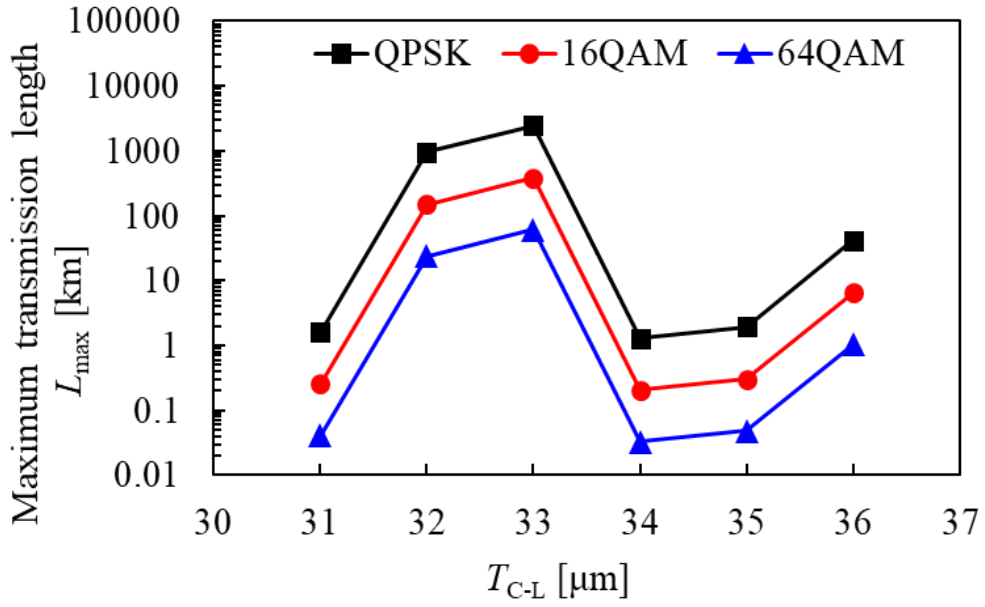

Fig.32. Maximum transmission distance L_{max} as a function of $T_{C\text{-}L}$

Conclusion

The core parameters of 4- and 6-core fibers used for designed fiber of the lowest XT value are summarized in Table VII, and the two largest types of inter-core XTs are also summarized in the table. We also evaluated the wavelength dependence of $XT_{02H\text{-}02L}$ (between the LP_{02} modes in both core H and core L) and $XT_{02H\text{-}21L}$ (between the LP_{02} mode in core H and the LP_{21} mode in core L) from 1530 nm to 1565 nm for C-band use in 4- and 6-core two-ring core layout Hetero-MCFs as shown in Fig. 33, where the fiber parameters are same as Table VII. The worst-case XT value of 6-core fiber is smaller than −40 dB/km, and the worst-case XT value

of 4-core fiber is also very low, indicating good performance in C-band use.

Table VII. Fiber parameters for designed 4LP-mode Hetero-MCFs

N	$T_{C\text{-}H}$ [μm]	$T_{C\text{-}L}$ [μm]	Λ [μm]	Λ_2 [μm]	$XT_{02H\text{-}02L}$ [dB/km]	$XT_{02H\text{-}21L}$ [dB/km]
4	31	32	43.9	61.0	−91.6	−112.0
6	31	33	30.6	51.1	−49.9	−59.9

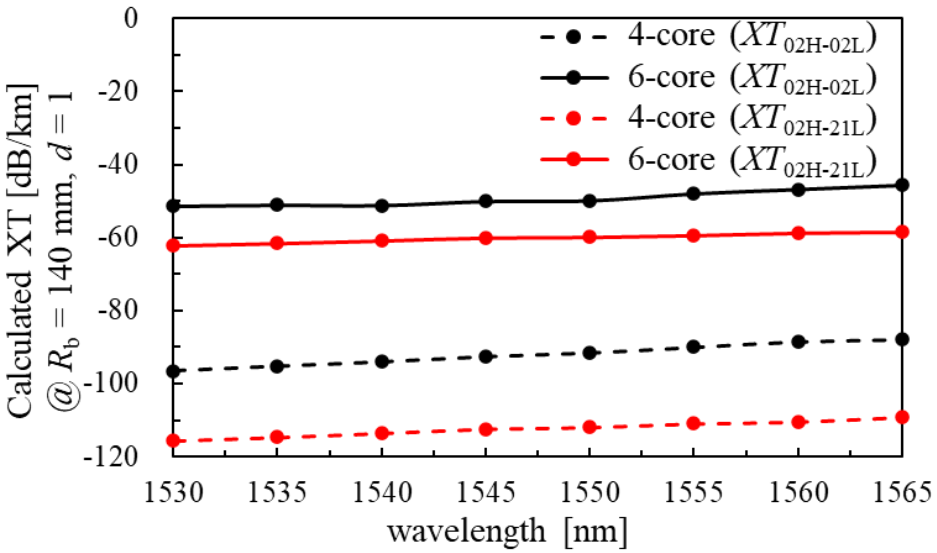

Fig. 33. C-band wavelength-dependent XT distribution in Hetero-MCFs with two-ring core layout, for N = 4 and 6, using parameters from Table VII.

The SCC assumes a pivotal role in elucidating the concurrent transmission capacity of MCFs, derived from the product of the number of cores and modes. Figure 34 serves as a visual representation, offering insights into the intricate relationship between SCC and inter-core XT for both 2LP-mode and 4LP-mode MCFs. Here, XT signifies the interference between the highest-order modes in adjacent cores, providing a crucial metric for assessing the fiber's performance.

In comparison to the insights presented in Chapter 3 of this study, the research findings showcased in this visualization demonstrate a notable and commendable enhancement in SCC, achieved concurrently with low XT levels. These findings not only underscore the feasibility of achieving higher simultaneous transmission capacities in MCFs but also highlight the potential for enhancing the overall performance of optical communication systems. As the demand for increased data

transmission capabilities continues to grow, the demonstrated enhancement in SCC with low XT positions MCF is a promising solution for the future development of high-capacity optical communication networks.

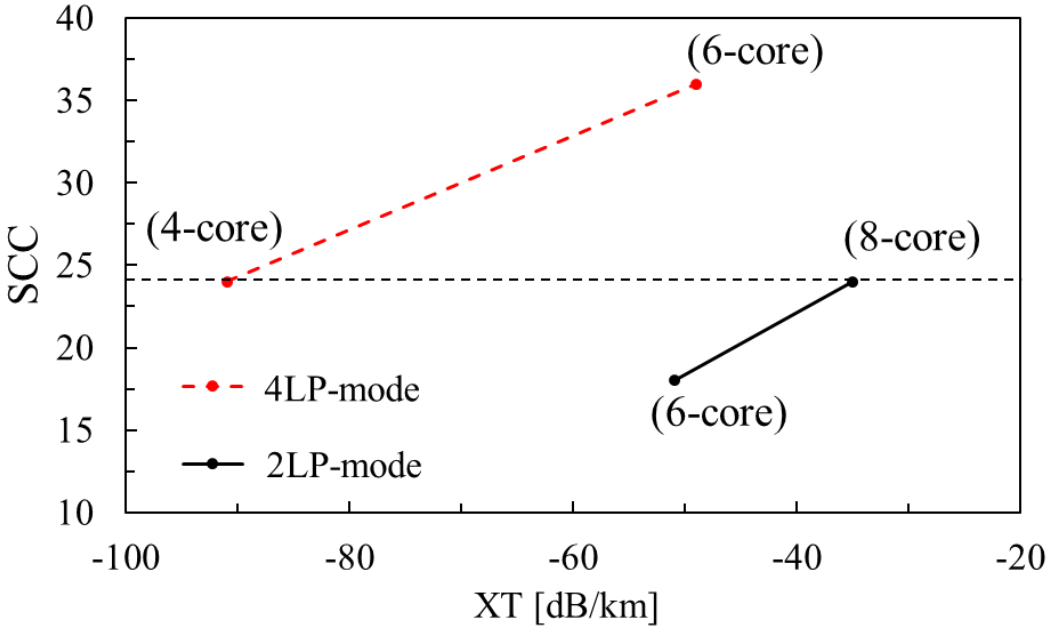

Fig. 34. Comparison of SCC and XT between 2LP- and 4LP-mode Hetero MCFs.

5.2 Two-ring core layout Hetero-SI-MCF for C+L band

Research on the C+L-band, in addition to existing C-band studies, is crucial due to the growing global demand for higher bandwidth and network capacity. The C+L band offers a broader spectrum, enabling more channels and enhancing long-distance communication efficiency. In this subsection, we explore the practicality of 2LP-mode MCFs within the C+L-band.

As detailed in Chapter 3, ensuring effective 2LP-mode transmission in the C-band requires the *BL* of the LP_{21} mode to exceed 1 dB/m at a wavelength of 1530 nm, while the *BL* of the LP_{11} mode should be below 0.01 dB/km at 1565 nm. In the context of the C+L-band, the cutoff for the LP_{21} mode's *BL* should also occur at 1530 nm, but the LP_{11} mode's *BL* needs to remain under 0.01 dB/km at a longer wavelength of 1625 nm. Figure 35 shows the general method of core selections.

Compared with Fig. 3 for the C-band, the solid line, which represents the LP_{11} mode's transmission limit, shifts upward as the upper boundary of the C+L-band is extended to 1625 nm.

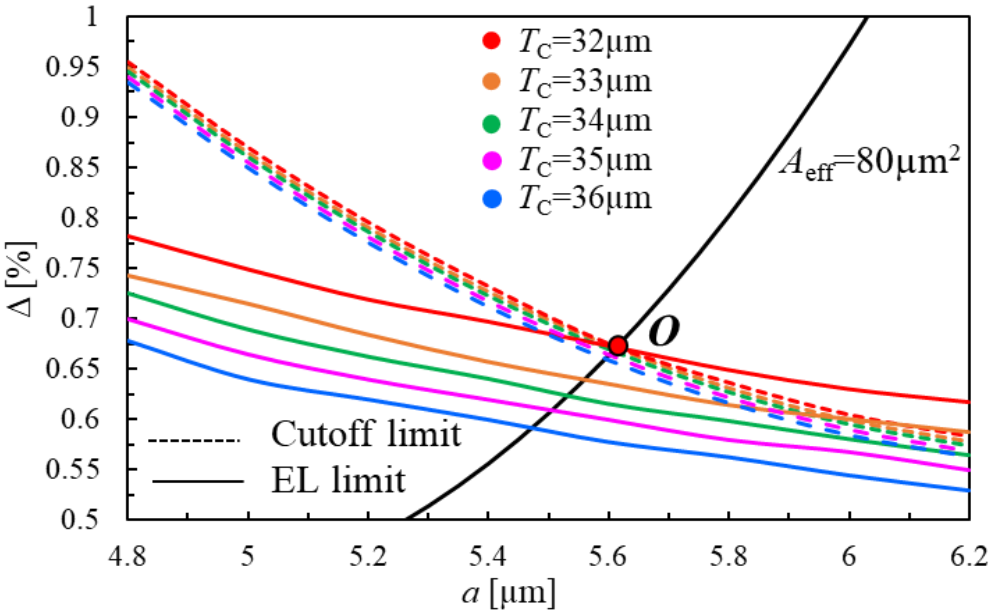

Fig. 35. Relationship between the core parameters and effective indices for the C+L-band.

Employing a process analogous to the one used for calculating XT, the XT distribution results, as depicted in Figure 36, shed light on the characteristic XT values. Notably, the findings unveil that the highest XT value is observed between the LP_{11} modes, specifically denoted as $XT_{11\text{-}11}$, for 2LP-mode Hetero-SI-MCFs designed to operate in the C+L-band.

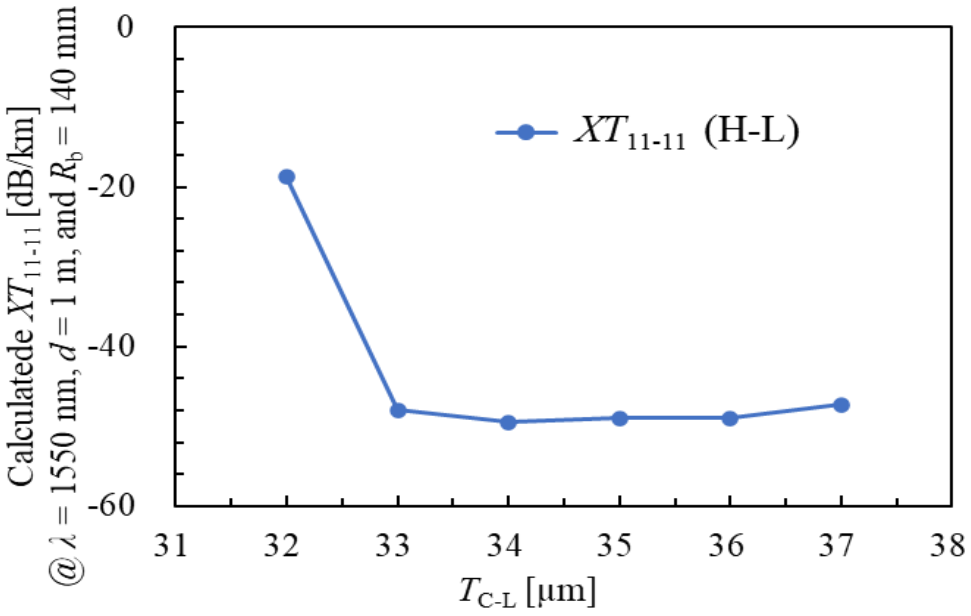

Fig. 36. Calculated $XT_{11\text{-}11}$ as functions of $T_{C\text{-}L}$ for C+L-band where $N = 6$, and $T_{C\text{-}H} = 32$ μm.

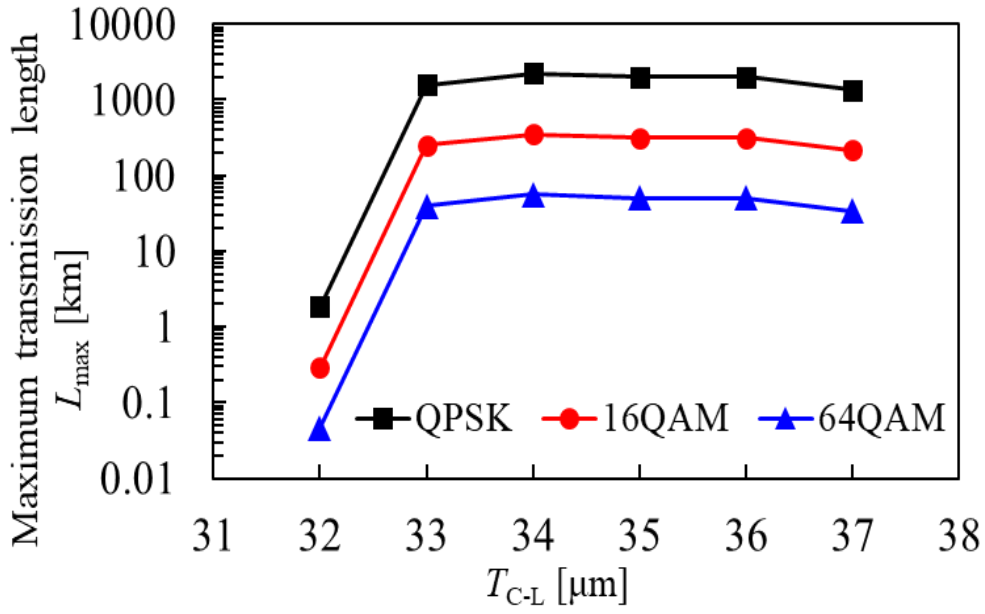

Fig. 37. Comparison of transmission length between the different format signals for Hetero-MCFs with the two-ring core layout for C+L-band.

Table VIII. Fiber parameters for designed 2LP-mode Hetero-MCFs for C+L-band

N	$T_{C\text{-}H}$ [μm]	$T_{C\text{-}L}$ [μm]	Λ [μm]	Λ_2 [μm]	$XT_{11\text{-}11}$ [dB/km]
6	32	34	29.6	49.4	−49.5

Fig. 37 shows the comparison of L_{max} between the Hetero-MCFs with the different format signals, corresponding to $XT_{11\text{-}11}$ for adjacent cores in Figs. 36, where $N = 6$. The 6-core fiber's L_{max} for QPSK reaches about 2200 km. The main parameters of the designed Hetero-SI-MCFs with the double-cladding structure for the C+L-band are listed in Table VIII. The cross-sectional view of the 6-core MCF with a two-ring core layout designed for the C+L-band is presented in Figure 38. We also evaluated the average XT distribution for C+L-band use (1530-1625 nm) of the LP_{11} mode of 6-core two-ring core layout Hetero-MCFs in Fig. 39. The worst-case XT value of 6-core fiber is feasible low, indicating good performance in C+L-band use.

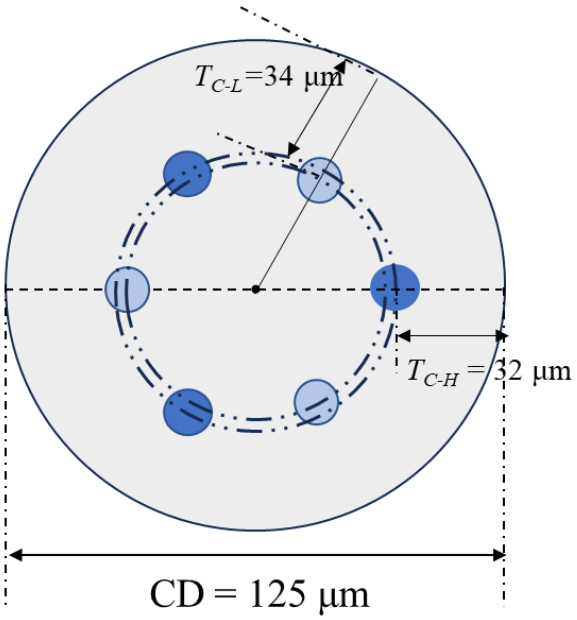

Fig. 38. Cross sections of the designed Hetero-SI-MCFs with double-cladding structure for C-band. (a) 6-core fiber. (b) 8-core fiber. (c) 10-core fiber.

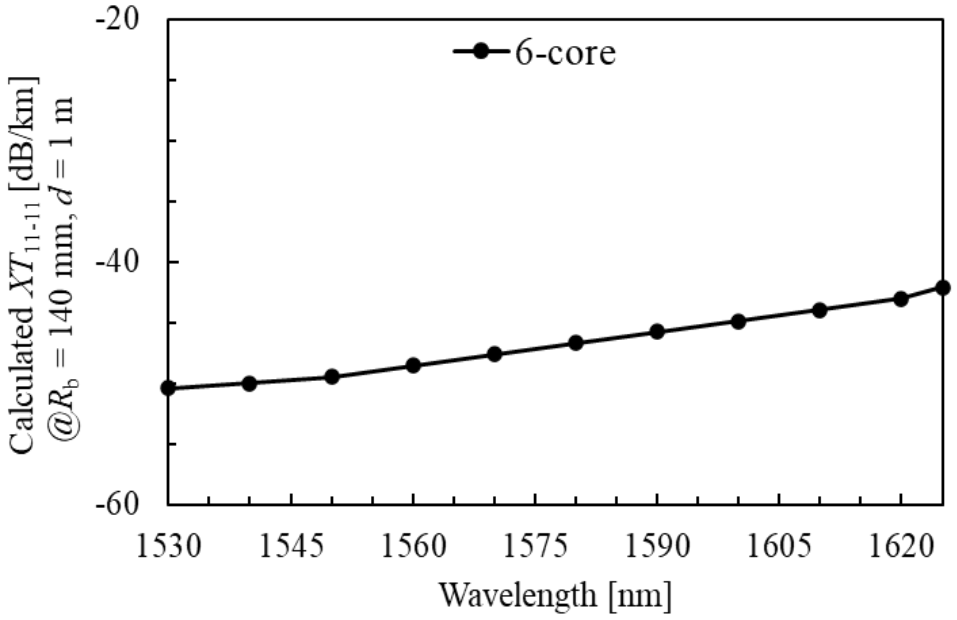

Fig. 39. C+L-band wavelength-dependent XT distribution in Hetero-MCFs with two-ring core layout, for N = 6, using parameters from Table VIII

Chapter 6. Summary

This comprehensive dissertation delves into the intricate relationship between mode coupling coefficients and inter-core XT within non-identical step-index (SI) cores, with a primary focus on the feasibility of designing 2LP mode Hetero-SI-MCFs within the confines of a standard 125 μm cladding diameter. Leveraging a straightforward SI distribution of refractive indices, the study successfully increases the core count to a maximum of 10, specifically tailored for C-band transmission.

A pivotal strategy employed in the research involves the implementation of a two-ring core allocation, proving highly effective in enhancing critical bending radius (R_{pk}) and reducing XT values in Hetero-SI-MCFs. The synergistic combination of this two-ring structure with C-band applications allows for the placement of a minimum of six and eight distinct cores within a 125 μm diameter, resulting in a substantial increase of 18 and 24, respectively, in the SCC. Furthermore, the study introduces a novel approach by integrating the two-ring structure with a double-cladding design. This innovation aims to mitigate loss in the outer cores of MCFs and facilitates an increase in the core count to ten. The double-cladding design incorporates a higher refractive index outer cladding, synergistically enhancing the core count.

In recognizing the limitations of merely increasing core numbers to enhance SCC, the research explores the viability of employing a two-ring structure in 4LP-mode Hetero-SI-MCFs within the standard 125 μm cladding diameter. The findings affirm that the two-ring structure excels in 4LP-mode MCF applications, maintaining exceptionally low XT values while concurrently increasing SCC.

Expanding the scope of the investigation, the research delves into preliminary examinations of fiber applications in the C+L bands. The study uncovers that the two-ring core layout effectively reduces inter-core XT in these bands, providing valuable insights for the future development of optical communication systems. The cumulative outcomes of this research not only contribute to a deeper understanding of MCF technologies but also lay a robust foundation for further optimizations in the dynamic field of optical communication.

References

[1] T. Morioka, “New generation optical infrastructure technologies: ‘EXAT Initiative’ Towards 2020 and Beyond,” Proc. Opt. Electron. Commun. Conf. (OECC), Paper FT4, July 2009.

[2] T. Mizuno, H. Takara, A. Sano and Y. Miyamoto, "Dense Space-Division Multiplexed Transmission Systems Using Multi-Core and Multi-Mode Fiber," J. Lightw. Technol., vol. 34, no. 2, pp. 582–592, Jan. 2016.

[3] Y. Amma, Y. Sasaki, K. Takenaga, S. Matsuo, J. Tu, K. Saitoh, M. Koshiba, T. Morioka, and Y. Miyamoto, “High-density multicore fiber with heterogeneous core arrangement,” Proc. Opt. Fiber Commun. Conf. (OFC), Paper Th4C.4, Mar. 2015.

[4] J. Sakaguchi, W. Klaus, J.M.D. Mendinueta, B.J. Puttnam, R.S. Luis, Y. Awaji, N. Wada, T. Hayashi, T. Nakanishi, T. Watanabe, Y. Kokubun, T. Takahata, and T. Kobayashi, “Realizing a 36-Core, 3-mode fiber with 108 spatial channels,” Proc. Opt. Fiber Commun. Conf. (OFC), Paper Th5C.2, Mar. 2015.

[5] K. Igarashi, D. Souma, Y. Wakayama, K. Takeshima, Y. Kawaguchi, T. Tsuritani, I. Morita, and M. Suzuki, “114 space-division-multiplexed transmission over 9.8-km weakly-coupled-6-mode uncoupled-19-core fibers,” Proc. Opt. Fiber Commun. Conf. (OFC), Paper Th5C.4, Mar. 2015.

[6] T. Sakamoto, T. Matsui, K. Saitoh, S. Saitoh, K. Takenaga, T. Mizuno, Y. Abe, K. Shibahara, Y. Tobita, S. Matsuo, K. Aikawa, S. Aozasa, K. Nakajima, and Y. Miyamoto, “Low-loss and low-DMD few-mode multi-core fiber with highest core multiplicity factor,” Proc. Opt. Fiber Commun. Conf. (OFC), Paper Th5A.2, Mar. 2016,

[7] S. Matsuo, K. Takenaga, Y. Sasaki, Y. Amma, S. Saito, K. Saitoh, T. Matsui, K. Nakajima, T. Mizuno, H. Takara, Y. Miyamoto, and T. Morioka, and J. Marciante, “High-spatial- multiplicity multicore fibers for future dense space-division- multiplexing systems,” J. Lightw. Technol., vol. 34, no. 6, pp. 1464–1475, Mar. 2016.

[8] T. Matsui, Y. Sagae, T. Sakamoto, and K. Nakajima, “Design and applicability of multi-core fibers with standard cladding diameter,” J. Lightw. Technol., vol.

38, no. 21, pp. 6065–6070, Nov. 2020.

[9] T. Hayashi, T. Nakanishi, K. Hirashima, O. Shimakawa, F. Sato, K. Koyama, A. Furuya, Y. Murakami, and T. Sasaki, “125-μm-cladding eight-core multi-core fiber realizing ultra-high-density cable suitable for O-band short-reach optical interconnects,” J. Lightw. Technol., vol. 34, no.1, pp. 85–92, Jan. 2016.

[10] P. J. Winzer, A. H. Gnauck, A. Konczykowska, F. Jorge, and J. Y. Dupuy, “Penalties from in-band crosstalk for advanced optical modulation formats,” Proc. Eur. Conf. Exhib. Opt. Commun. (ECOC), Paper Tu.5.B.7, Sep. 2011.

[11] K. Takenaga, Y. Sasaki, N. Guan, S. Matsuo, M. Kasahara, K. Saitoh, and M. Koshiba, “Large effective-area few-mode multicore fiber,” Opt. Lett., vol. 24, no. 21, pp. 1941–1944, Nov. 1, 2012.

[12] K. Saitoh, T. Matsui, T. Sakamoto, M. Koshiba, and S. Tomita, “Multi-core hole-assisted fibers for high core density space division multiplexing,” Proc. Opt. Electron. Commun. Conf. (OECC), Paper 7C2-1, July. 2010.

[13] X. Xie, J. Tu, K. Long, and K. Saitoh, “Heterogeneous 32-core fiber with square-lattice layout for high-density transmissions,” Proc. Asia Commun. Photon. Conf. (ACP), Paper AS2A, Nov. 2016.

[14] Y. Sasaki, M. Ozeki, K. Takenaga, and K. Aikawa, “Asymmetrically arranged 8-core fibers with center core suitable for side-view alignment in datacenter networks,” Proc. Opt. Fiber Commun. Conf. (OFC), Paper T4J.1, Feb. 2020.

[15] Y. Wang, T. Fujisawa, Y. Sagae, T. Sakamoto, T. Matsui, K. Nakajima, and K. Saitoh, “A Novel Core Allocation in Heterogeneous Step-Index Multi-Core Fibers with Standard Cladding Diameter,” J. Lightw. Technol., vol. 39, no.22, pp. 7231–7237, Nov. 2021.

[16] Y. Sagae, T. Matsui, T. Sakamoto, T. Iwaya, T. Mori, T. Sato, K. Saitoh, and K. Nakajima, “A 125-μm CD uncoupled 3-mode 4-core fibre with the highest core multiplicity factor,” Proc. Eur. Conf. Exhib. Opt. Commun. (ECOC), paper Tu3A.2, Sep. 2022.

[17] T. Matsui, T. Sakamoto, Y. Goto, K. Saito, K. Nakajima, F. Yamamoto, and T. Kurashima, “Design of 125 μm cladding multi-core fiber with full-band compatibility to conventional single-mode fiber,” Proc. Eur. Conf. Exhib. Opt. Commun. (ECOC), paper We1.4.5, Sep. 2015.

[18] T. Hayashi, T. Nakanishi, K. Hirashima, O. Shimakawa, F. Sato, K. Koyama,

A. Furuya, Y. Murakami, T. Sasaki, “125-μm-Cladding Eight-Core Multi-Core Fiber Realizing Ultra-High-Density Cable Suitable for O-Band Short-Reach Optical Interconnects,” J. Lightw. Technol., vol. 34, no. 1, pp. 85-92, Jan. 2016.

[19] T. Gonda et al., “5-core fibre with heterogeneous design suitable for migration from single-core system to multi-core system,” Proc. Eur. Conf. Opt. Commun. (ECOC), Paper W.2.B.1, Sep. 2016.

[20] S. Nozoe, R. Fukumoto, Y. Amma, T. Sakamoto, T. Matsui, K. Takenaga, Y. Abe, K. Tsujikawa, N. Hanzawa, S. Aozasa, K. Aikawa, M. Ohashi, and K. Nakajima, “Ultra-Low Crosstalk 125-μm-Cladding Four-Hole Four-Core Fibers Fabricated by the Over-Cladding Bundled Rods Method,” J. Lightw. Technol. Vol. 37, no.21, pp. 5600-5608, Aug. 2019.

[21] T. Sakamoto, S. Aozasa, T. Mori, M. Wada, T. Yamamoto, S. Nozoe, Y. Sagae, K. Tsujikawa, and K. Nakajima, “Twisting-Rate-Controlled 125 μm Cladding Randomly Coupled Single-Mode 12-Core Fiber,” J. Lightw. Technol. vol. 36, no. 2, pp. 325-330, Aug. 2018.

[22] S. Jiang, L. Ma, M. N. Velazquez, Z. He, and J. K. Sahu, “Optimized design of 125-μm 6-core fiber with large effective area for wideband optical transmission,” in CLEO-PR. Conf. Paper Th2E.3, Aug. 2018.

[23] S. Nozoe, R. Fukumoto, T. Sakamoto, T. Matsui, Y. Amma, K. Takenaga, K. Tsujikawa, S. Aozasa, K. Aikawa, and K. Nakajima, “Low Crosstalk 125 μm-Cladding Multi-Core Fiber with Limited Air-Holes Fabricated with Over-Cladding Bundled Rods Technique,” Proc. Opt. Fiber Commun. Conf. (OFC), Paper Th1H.6, Mar. 2017.

[24] M. Koshiba, K. Saitoh, and Y. Kokubun, “Heterogeneous multi-core fibers: Proposal and design principle,” IEICE Electron. Exp., vol. 6, no.2, pp. 98–103, Jan. 2009.

[25] T. Hayashi, T. Taru, O. Shimakawa, T. Sasaki, and E. Sasaoka, “Design and fabrication of ultra-low crosstalk and low-loss multi-core fiber,” Opt. Exp., vol. 19, no.17, pp. 16576–16592, Aug. 2011.

[26] M. Koshiba, K. Saitoh, K. Takenaga, and S. Matsuo, “Analytical expression of average power-coupling coefficients for estimating intercore crosstalk in multicore fibers,” IEEE Photonics J., vol. 4, no.5, pp. 1987–1995, Oct. 2012.

[27] K. Saitoh, “Multi-Core Fiber Technology for SDM: Coupling Mechanisms and

Design,” J. Lightw. Technol., vol. 40, no.5, pp. 1527–1543, Mar. 2022.

[28] M. Koshiba, K. Saitoh, K. Takenaga, and S. Matsuo, “Multi-core fiber design and analysis: Coupled-mode theory and coupled-power theory,” Opt. Exp., vol. 19, no. 26, pp. B102–B111, Dec. 2011.

[29] K. Okamoto, Fundamentals of Optical Waveguides, 2nd ed. (Academic Press. 2006).

[30] T. Fujisawa, Y. Amma, Y. Sasaki, S. Matsuo, K. Aikawa, K. Saitoh, and M. Koshiba, “Crosstalk analysis of heterogeneous multicore fibers using coupled-mode theory,” IEEE Photon. J., vol. 9, no. 5, pp. 1–8, Oct. 2017.

[31] K. Takenaga, Y. Arakawa, Y. Sasaki, S. Tanigawa, S. Matsuo, K. Saitoh, and M. Koshiba, “A large effective area multi-core fiber with an optimized cladding thickness,” Opt. Exp., vol. 19, no. 26, pp. 543–550, Dec. 2011.

[32] T. Hayashi, T. Taru, O. Shimakawa, T. Sasaki, and E. Sasaoka, “Low-crosstalk and low-loss multi-core fiber utilizing fiber bend,” Proc. Opt. Fiber Commun. Conf. (OFC), Paper OWJ3, Mar. 2011.

[33] K. Saitoh, and M. Koshiba, “Full-vectorial imaginary-distance beam propagation method based on a finite element scheme: Application to photonic crystal fibers,” IEEE J. Quantum Electron., vol. 38, no. 7, pp. 927–933, Jul. 2002.

[34] S. Nozoe, T. Sakamoto, T. Matsui, Y. Amma, K. Takenaga, Y. Abe, K. Tsujikawa, S. Aozasa, K. Aikawa, and K. Nakajima, “125 μm-cladding 2LP-mode and 4-core multi-core fibre with air-hole structure for low crosstalk in C+L band,” Proc. Eur. Conf. Opt. Commun. (ECOC), Paper Tu3A.2, Sep. 2017.

Acknowledgments

Throughout the development of this paper, I received invaluable guidance and encouragement from start to finish. My deepest thanks go to Professor Kunimasa Saitoh from the Information and Communication Photonics Laboratory, Department of Media Network, at the Graduate School of Information Science and Technology, Hokkaido University. I am equally grateful to Associate Professor Takeshi Fujisawa of the same laboratory for his passionate mentorship. Additionally, I extend my sincere appreciation to Associate Professor Takanori Sato for his detailed advice and strong support during our meetings.

I also wish to acknowledge Prof. Takeo Ohgane and Prof. Toshihiko Nishimura for their constructive suggestions and guidance in my research.

Lastly, I am truly thankful to all members of the laboratory for their valuable insights and advice that enriched my daily research.

Research Achievements

Journals

[1] **Z. Zhao**, Y. Wang, T. Sato, T. Fujisawa, and K. Saitoh, “Investigation of heterogeneous step-index 2LP-mode multi-core fibers based on a two-ring layout with standard cladding diameter,” Opt. Continuum, vol. 2, no. 5, pp. 1137-1147 (2023).

[2] **Z. Zhao**, T. Sato, T. Fujisawa, T. Iwaya, Y. Sagae, T. Sakamoto, T. Matsui, K. Nakajima, and K. Saitoh, “Investigation of double-cladding heterogeneous step-index 2LP-mode multicore fiber with a two-ring layout,” J. Opt. Soc. Am. B, vol. 40, no. 10, pp. 2511-2518 (2023).

Conference papers

[1] **Z. Zhao**, T. Sato, T. Fujisawa, T. Iwaya, Y. Sagae, T. Sakamoto, T. Matsui, K. Nakajima, and K. Saitoh, “Design of Double-Cladding Heterogeneous 2LP-Mode 6-Core Fiber with Two-Ring Layout,” Opto-Electronics and Communications Conference (OECC), Paper OECC2023-0317-7, Shanghai, China, July 2-6 (2023).

[2] **Z. Zhao**, Y. Wang, T. Sato, T. Fujisawa, and K. Saitoh, “Design of Heterogeneous 4LP-Mode Multicore Fiber with Two-Ring Layout”, Asia Communications and Photonics Conference (ACP), Paper ACPPOEM-0726-16, Wuhan, China, Nov. 4-7 (2023).